Improvements in Superconducting Magnetometry

Zur Erlangung des akademischen Grades eines

Doktors der Naturwissenschaften (Dr. rer. nat.)

von der KIT-Fakultät für Physik
des Karlsruher Instituts für Technologie (KIT)

angenommene
Dissertation

von

(M. Sc.) Michael Schulze

Tag der mündlichen Prüfung: 21. April 2023
Erster Gutachter: Prof. Dr. Wolfgang Wernsdorfer
Zweiter Gutachter: Prof. Dr. Mario Ruben

Zusammenfassung

In dieser Arbeit wird die Erweiterung des Magnetometrieaufbaus auf der Grundlage supraleitender Quanteninterferenzgeräte untersucht. Die Untersuchung und Charakterisierung von Einzelmolekülmagneten bildet die Grundlage für den Einsatz dieser Systeme in der Quantensensorik und im Quantencomputing. Zur Erhöhung der Stabilität bei höheren Temperaturen und angelegten Magnetfeldern werden neue Bauelemente auf der Basis von Niobnitrid vorgestellt und charakterisiert. Eine abschließende Demonstration zeigt die Eignung für magnetometrische Messungen. Die Erweiterung zur Kombination von Hochfrequenzstrahlung und Magnetometrie bildet die Grundlage für die resonante und kohärente Manipulation des Eigenspins dieser Systeme. Hierfür werden ein neuer Probenhalter und ein koplanarer Wellenleiter auf dem Chip hergestellt, charakterisiert und eingesetzt. In einer abschließenden Anwendung wird dieser Aufbau in einem kombinierten Experiment zur elektonischen paramagnetischen Resonanz und Magnetometrie eingesetzt. Zur Untersuchung eines neu synthetisierten Einzelmolekülmagneten auf der Basis des Gd3+-Ions wird die resonante Anregung der Elektronenspinzustände genutzt, um die Energieniveaus in Abhängigkeit vom angelegten Magnetfeld abzubilden. Dies wird verwendet, um die Wirkung der organischen Liganden auf das Ion zu beschreiben, das in einem Satz von Ligandenfeldparametern zusammengefasst ist.

Abstract

This thesis explores the extension of the magnetometry setup based on Superconducting QUantum Interference Devices. The study and characterization of single molecule magnets provides the basis in using these systems in quantum sensoric and quantum computing applications. For increased stability at higher temperatures and applied magnetic fields, new devices based on niobium nitride are introduced and characterized. A final demonstrations shows the suitability for magnetometry measurements. The extension to combine radio frequency radiation and magnetometry provides the basis for resonant and coherent manipulation of the inherent spin of these systems. For this a new sample holder and on-chip coplanar waveguide are fabricated, characterized and applied. In a final application, this setup is applied in a combined electon paramagnetic resonance and magnetometry experiment. To investigate a newly synthesized single molecule magnet based on the Gd3+ ion, resonant excitation of the electron spin states is used to map the energy levels depending on the applied magnetic field. This is used to describe the effect of the organic ligands on the ion summarized in a set of ligand field parameters.

Contents

1. Introduction

While magnetism has been known for thousands of years [1], this phenomenon has been investigated in bulk materials showing long-range magnetic order resulting from local exchange interaction. The resulting magnetic properties, such as remanence and hysteresis, stem from the collective behavior of all atoms in the material. On the other hand, the demonstration of bistable large magnetic moments has been a recent development in the last two decades. As a result, this new group of chemical compounds has been named single-molecule magnets (SMMs).

The advent of single-molecule magnetism is marked with the discovery of the large magnetic moment and magnetic bistability of the molecular cluster $Mn_{12}O_{12}(CH_3COO)_{16}(H_2O)_4$ (Mn_{12}-ac) [2, 3]. This was followed by breakthrough observations of quantum tunneling of magnetization (QTM) [4, 5] in Mn_{12}-ac, ground state quantum tunneling [6], and topological quantum phase interference effects in $[Fe_8O_2(OH)_{12}(tacn)_6]^{8+}$ (Fe_8) [7]. To this day, these systems remain the most investigated [8, 9].

The properties of SMMs are based on an inner core of magnetic ions embedded in a shell of organic ligands. This broad definition covers molecules with a wide range of shapes and sizes. Selective substitution of ligands and ions allows the separate altercation of the coupling to the environment with different ligands and the magnetic properties based on the ions.

Current research focuses on integrating molecular structures in quantum information processing as memory units and quantum digits (qudits). Utilization as the latter has been demonstrated by demonstrating the Grover algorithm using the nuclear spin states of the $TbPc_2$ SMM [10]. This is supported by the monodisperse properties, as chemical synthesis yields many molecules with identical properties. As a result, the formation of monocrystals allows the amplification of the magnetic properties and access to single molecular properties from measurements performed on ensembles. The investigation of ensembles allows the characterization of potential candidates for quantum

memory units. The results obtained pave the way to understanding and using them in further advanced applications.

Satisfying this interest requires the usage of highly sensitive magnetometry. Among various low-temperature techniques, exploiting the quantum properties of superconducting circuits, μ-SQUID magnetometry allows the most detailed study of magnetization [11–19]. Based on nanometer-sized constriction in a micrometer-sized superconducting loop, these superconducting circuits, called Superconducting Quantum Interference Devices (SQUIDs), provide sensitivities down $10^{-5}\,\Phi_0/\sqrt{\text{Hz}}$ and $10^{-4}\,\Phi_0/\sqrt{\text{Hz}}$ for aluminum and niobium based systems respectively [20].

To provide the theoretical background for these systems, the basic principles of superconducting circuits are explained in Chapter 2. Explaining the basic principles of superconductivity and the superconducting circuit elements Josephson junction and SQUIDs help the understanding of this measurement method and the results of Chapter 5.

The basic principles of single-molecule magnetism are shown in Chapter 3, as these are needed to understand all magnetization measurements.

The low temperatures required to observe single-molecule magnetism are provided by the Sionludi dilution cryostat. This low-temperature setup with the periphery for the measurements is explained in Chapter 4.

To investigate single-molecule magnets with high blocking temperatures and other small magnetic objects with exciting features such as the superconducting transition of niobium nano-particles, a new magnetic sensor based on the superconductor niobium nitride has been fabricated and tested, as shown in Chapter 5.

To explore the strength of combining magnetometry and exciting spin systems with electromagnetic radiation in the GHz-range a new chip carrying SQUIDs and an on-chip coplanar waveguide has been fabricated and tested, as described in Chapter 6.

Finally, one application, performing electron paramagnetic resonance (EPR) on an SMM based on a Gd^{3+} is shown in Chapter 7 to show the capabilities and strength of this technique.

2. Superconducting Circuits

As the work of this thesis is based on superconducting circuits, called SQUIDs, for magnetometry measurements, this Chapter will provide a brief theoretical foundation to understand both characterization of these devices in Chapter 5 and functionality used in Chapters 6 and 7. For this, Section 2.1 will review the basic principles of superconductivity. As most of the results of Chapter 5 can be reduced to the properties of one circuit element, the Josephson junction, this will be discussed in Section 2.2. Combining several of these can form a SQUID, whose functionality will be discussed in Section 2.3.

2.1. Superconductivity

Superconductors present a class of materials that present extraordinary at low temperatures. Below a critical phase transition temperature T_c, the direct current resistance of a superconductor drops at least 14 orders of magnitude to an unmeasurable small value, first discovered by H. Kamerlingh Onnes [21, 22]. Furthermore, superconductors exhibit perfect diamagnetism by expelling all magnetic fields in the superconducting state, as discovered by W. Meissner and R. Ochsenfeld [23].

The first theoretical description was introduced by Bardeen, Cooper, and Schrieffer in 1957, later denoted as the BCS-theory [24]. Several textbooks, such as [25], provide a detailed description of the theory. The theory is based on an attractive interaction between electrons, allowing the coupling into bosonic Cooper pairs, condensing into a common ground state. The wave function ψ can be defined at every point $(\vec{r})$ by the density of Cooper pairs n_s and a global phase ϕ as

$$\psi(\vec{r}) = \sqrt{n_s(\vec{r})}\mathrm{e}^{i\phi(\vec{r})} \tag{2.1}$$

As this macroscopic wave function describes all Cooper pairs, they exhibit coherent behavior. As a result of the global phase of the wave function is the quantization of magnetic flux, which can penetrate a superconducting loop. While the wave function is exactly defined at every position on the loop, a change of the phase of multiples of 2π does not change the wave function. Thus the change of phase $\Delta\phi$ can only vary by $n \cdot 2\pi$ for a closed contour around the loop, with n being an integer number. The phase variation is connected by the vector potential $\vec{A}$ to the magnetic flux Φ penetrating the loop by:

$$\frac{\hbar}{2e}\Delta\phi = \frac{\hbar}{2e}\oint \nabla\phi \mathrm{d}\vec{l} = \oint \vec{A}\mathrm{d}\vec{l} = \int \vec{B}\mathrm{d}\vec{S} = \Phi, \tag{2.2}$$

using the reduced Planck constant $\hbar = h/2\pi$ and l and S as the circumference and area of the loop respectively. Considering the magnetic flux quantum $\Phi_0 = h/2e = 2.07 \times 10^{-15}$ Wb, shows, the the flux Φ penetrating a superconducting loop can only be a multiple of Φ_0.

Another approach to describe superconductivity can be made using the Ginzburg-Landau theory for second-order phase transitions [25]. The Cooper pair density is the order parameter $\psi(\vec{r})$. While the theory will not be discussed here, the importance of coherence length ξ will be highlighted. Changes of ψ due to a local disturbance, e.g., at the surface of a superconductor, occur over a length ξ, which is usually in the order of up to hundreds of nanometres [26]. This limitation on the dimensional change of superconductivity allows the induction of superconductivity in non-superconducting materials close to the surface of a superconductor.

2.2. The Josephson Junction

The Josephson junction poses one of the most important elements in superconducting circuits, as the underlying Josephson effect demonstrates the coherence of the superconducting condensate. This Section provides a short overview of the Josephson effect and the realization of Josephson junctions.

In 1962, Josephson derived two theoretical predictions for the transport through an insulating tunnel barrier between two superconducting electrodes [27]:

A supercurrent I_S can flow between the electrodes without resistance and the corresponding voltage drop. The supercurrent only depends on the phase difference $\varphi = \phi_1 - \phi_2$ of the superconducting condensate between the electrodes by:

$$I_S = I_0 \sin \varphi \tag{2.3}$$

where the critical current I_0 is a junction-specific property depending on geometry, intrinsic properties, and temperature. This relationship is usually referred to as the DC-Josephson effect. on the other hand, a change in the phase difference over time causes a voltage drop across the junction:

$$\frac{\mathrm{d}\varphi}{\mathrm{d}t} = \frac{2e}{\hbar} V. \tag{2.4}$$

As the combination of (2.3) and (2.4) show, an oscillating current causes a constant voltage across the junction. Hence, (2.4) is often referred to as AC-Josephson effect. as I_S has to be a gauge-invariant quantity, φ has to be replaced by the gauge-invariant phase difference δ in (2.3) and (2.4) [25]:

$$\delta = \varphi - \frac{2\pi}{\Phi_0} \int \vec{A} \mathrm{d}\vec{s}. \tag{2.5}$$

The direction of the integration goes from one electrode to the other. Furthermore, (2.5) explains the appearance of the Fraunhofer modulation of I_S for a magnetic field applied in parallel to the barrier.

Even though these predictions are based on a superconductor-insulator-superconductor junction, they hold in general for many other types of junctions with minor changes. The junctions require a non-vanishing superconducting gap across the junction and a reduction of the critical current is smaller than for the electrodes. Therefore, the weak link can be formed by normal metal or semiconductor, a constriction in the superconductor or a carbon nanotube [28]. Examples are shown in Figure 2.1.

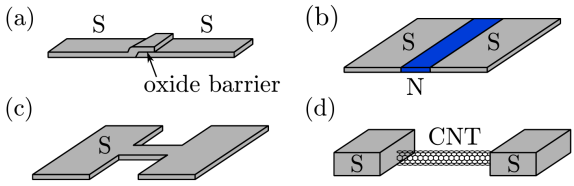

Figure 2.1. – Different types of Josephson junctions. a) Insulating tunnel barrier b) Normal metal weak link c) Superconducting constriction d) Carbon nanotube. Adapted from [29].

The RCSJ-Model

The switching of a Josephson junction to the resistive state can be done in the frame of the Resistively and Capacitively Shunted Junction (RCSJ-) model, which will be introduced here. This description is based on [25].

The model is based on a representation via an equivalent circuit to describe a JJ. The dissipative transport of quasi-particles gets represented by a resistor R, which is parallel to the ideal Josephson junction. The capacitance C in between the superconducting electrodes gets included as well. Figure 2.2a shows the resulting equivalent circuit. Using the first Josephson equation and Kirchhoff's current law results in the differential equation

$$I = I_0 \sin(\delta) + V/R + C\frac{\mathrm{d}V}{\mathrm{d}t} \tag{2.6}$$

with the bias current I flowing through the junction and the voltage drop V across the junction. Inserting the second Josephson equation into 2.6, leads to

$$\frac{1}{\omega_P^2}\frac{\mathrm{d}^2\delta}{\mathrm{d}t^2} + \frac{1}{\omega_P^2 RC}\frac{\mathrm{d}\delta}{\mathrm{d}t} + \sin\delta = \frac{I}{I_0} \tag{2.7}$$

using the self-resonance frequency $\omega_P = \sqrt{2eI_0/\hbar C}$, called the plasma frequency.

An intuitive understanding of this differential equation can be reached by comparing it with the differential equation for a particle of mass m in a tilted washboard potential $U(x) = -U_0 \cos x - U_1 x$ with damping:

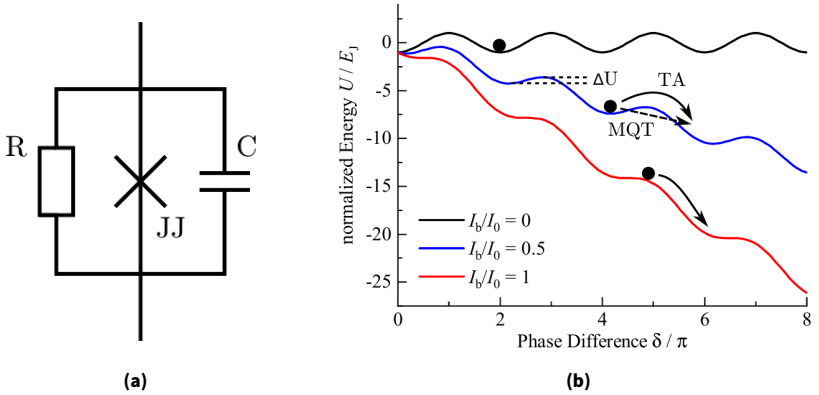

Figure 2.2. – a) The equivalent circuit of a Josephson junction, which is used in the RCSJ model. Parallel to the ideal Josephson junction is the resistor R to account for the dissipative transport of quasiparticles and the capacitance C between the superconducting leads. b) In the RCSJ model, the switching of a Josephson junction gets visualized by the escape of a particle from a washboard potential. As the position of the particle represents the phase change across the junction, a monotonous movement equals a voltage drop across the junction. The tilt of the potential changes with the applied bias current, resulting in the vanishing of the potential barrier ΔU. The barrier can be overcome by escape through thermal activation (TA) or macroscopic quantum tunneling (MQT).

$$m\frac{\mathrm{d}^2x}{\mathrm{d}t^2} = -U_0 \sin x + U_1 - \gamma\frac{\mathrm{d}\delta}{\mathrm{d}t} \tag{2.8}$$

In this comparison, the so-called "phase particle" position corresponds to the phase difference between the two superconducting leads. Furthermore the comparison of Equation 2.7 and Equation 2.8 provides the mass $m = \left(\frac{\hbar}{2e}\right)^2 C$, the damping factor $\gamma = \left(\frac{\hbar}{2e}\right)^2 \frac{1}{R}$, and the potential

$$U(\delta) = -\frac{\hbar I_0}{2e}\left(\cos\delta + \frac{I}{I_0}\delta\right) = -E_J\left(\cos\delta + \frac{I}{I_0}\delta\right) \tag{2.9}$$

with E_J being the so call Josephson coupling energy. The potential is shown in Figure 2.2b. The equilibrium for zero applied bias current consists of the particle residing in one of the minima, oscillating at a frequency proportional

to ω_P. Equation 2.9 shows that an applied bias current I tilts the potential and decreases the barrier height ΔU. For I reaching I_0, ΔU vanishes. Close to this point, ΔU can be approximated by

$$\Delta U(I) \approx \left(1 - \frac{I}{I_0}\right)^{3/2} \tag{2.10}$$

using $U_0 = 2E_J$. According to the second Josephson equation, the phase difference δincreases continuously with the barrier disappearing, resulting in a voltage drop across the junction. As a result, the resistivity jumps to a finite, measurable value.

Although the barrier only vanishes for $I = I_0$, the particle tends to cross the barrier at currents smaller than I_0 due to tunneling or thermal activation, which will be discussed in Section 2.2.

It is important to note that the current-phase relation is not required to be sinusoidal [30], especially for an array of junctions, which can show almost a sawtooth-like shape[31]. While this changes the shape of the potential in the model, the qualitative behavior of the junction stays unchanged.

When reducing the bias current below I_0, the particle can be trapped again in one of the potential wells, called retrapping. This dynamic is strongly influenced by the quality factor

$$Q = \omega_P RC \tag{2.11}$$

of the junction [25]. The junction is underdamped if $Q > 1$ and overdamped for $Q < 1$. This becomes clearer when considering the retrapping process. Starting with a junction, which has switched to the resistive state at $I > I_0$, the particle runs down the potential. If I drops below I_0, a finite barrier appears. The damping quickly dissipates the energy for an overdamped junction, and the particle gets retrapped at I close to I_0.

The underdamped junction keeps the kinetic energy above the barrier height, even at much smaller currents. Here, the retrapping occurs at [25]

$$I_r = \frac{4I_0}{\pi Q} \tag{2.12}$$

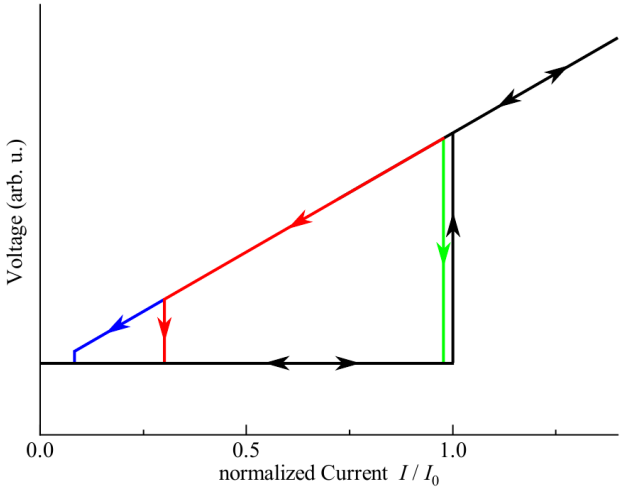

Figure 2.3. – I-V curves for an overdamped (green) and underdamped (red) junction as well as for a small weak link subject to heating (blue). Increasing the bias current leads to a switching of the junction to the resistive state at $I = I_0$. Ramping down the bias current after the switching event leads to a retrapping of the particle in the RCSJ model. For an overdamped junction, this happens at $I_r \approx I_0$, as a small barrier is sufficient to retrap the particle. The retrapping happens at much lower currents as the particle's kinetic energy dissipates much slower in an underdamped junction. Heating in nm-sized weak links further decreases the retrapping current. Adapted from [29].

As a result, the I-V shows a hysteresis. In small junctions, the delayed dissipation of heat accumulated in the resistive state prevents retrapping at the value defined in (2.12) [32]. The particle can get retrapped only at smaller bias currents after the junction cooled down sufficiently. Figure 2.3 shows examples of over- and underdamped junctions and junctions subject to heating.

Thermal Activation and Macroscopic Quantum Tunneling

As already mentioned, the switching of a Josephson Junction can be described by the escape of a particle over a barrier. This process gets enhanced at nonzero temperatures by thermal activation (TA). The escape rate is given by the Arrhenius law for $k_B T \ll E_J$ [25]

$$\Gamma(T, I) = \Gamma_0(I) \exp - \left(\frac{\Delta U(I)}{k_B T} \right) \tag{2.13}$$

using the potential barrier ΔU and the Boltzmann constant k_B. While ΔU of a tunneling junction is given by (2.10), (2.13) holds for arbitrarily shaped junctions as long as $\Delta U \gg k_B T$ is satisfied. As Γ_0 gives the frequency with which the particle tries to escape the well, it is called the attempt frequency. For a moderately damped junction, the plasma frequency $\omega_P/2\pi$, given by the potential curvature, is in the same order of magnitude as Γ_0. For a tunnel junction Γ_0 depends on I as

$$\Gamma_0(I) \propto \left(1 - \frac{I}{I_0} \right)^{1/4} \tag{2.14}$$

TA allows switching of the junction for bias currents below I_0, leading to a distribution of the switching events as a function of the bias current. The corresponding current is called switching current I_{sw}.

Kurkijärvi performed the first theoretical predictions for this thermally activated escape of a particle over a barrier, dependent on an applied field (bias current for the case of Josephson junction) [33]. Fulton and Dunkelberger did the first measurements on thermally activated transitions to the resistive state. The results did show good agreement between experimental results and theory [34].

At low temperatures, the tunneling through the barrier dominates over thermally assisted switching. This is called macroscopic quantum tunneling (MQT) [35]. Here, the picture of a classical particle breaks down, but the picture of a wave function extending through the barrier has to be applied [36]. This effect has been shown in Nb tunnel junctions by Voss and Webb [37], and Clarke et al. in Nb-NbOx-PbIn junctions [36]. The MQT escape rate can also be modeled with the Arrhenius law by using an effective escape temperature T_{esc} for the temperature-independent tunneling process instead of T.

The Model of Kurkijärvi for Switching Current Distributions

The model of Kurkijärvi for switching current distributions provides the theoretical basis to understand the thermally activated escapes over a bias field-dependent barrier. This will be the ground for understanding the measurements presented in 5. While the calculations were originally done for flux in a superconducting loop [33], these can be used for the switching of Josephson junctions as well, as both describe the escape from a potential well.

For $\Delta U \gg k_B T$, the escape rate is given by (2.14), while for switching at bias currents close to I_0, the barrier height can be approximated by (2.10). In case every escape of the phase particle from the well leads to a free-running particle, the switching rate is equal to the escape rate. It is important to note that in the presented measurements, the switching events are stochastic and independent. Therefore, the probability that a junction did not switch after a time t is given by

$$W(t) = \exp\left(-\int_0^t \Gamma(I(t'))\mathrm{d}t'\right). \tag{2.15}$$

Experiments are often conducted at a constant sweeping rate $\dot{I}$ of I and sweeping times much larger than the inverse attempt frequency. As a result, we can modify (2.15) by substituting t' with I'

$$W(I) = \exp\left(-\frac{1}{\dot{I}}\int_0^t \Gamma(I')\mathrm{d}I'\right). \tag{2.16}$$

As a result, we get the probability $P(I)$ for the junction to switch at a defined value of I as the derivative of (2.16)

$$P(I) = -\frac{\mathrm{d}W(I)}{\mathrm{d}I} = \frac{\Gamma(I)}{\dot{I}}W(I). \tag{2.17}$$

This shows that $P(I)$ is the product of switching in the interval $[I, I + \Delta I]$ and not switching before I. To get an analytical expression, $\Delta U(I)$ can be linearized [38]. Inserting this linearization into Equation 2.13 gives the Gumbel-distribution

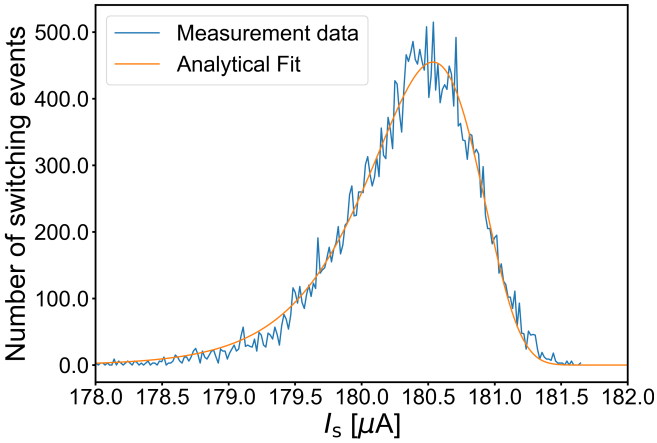

Figure 2.4. – Histogram of switching currents measured on an NbN-SQUID, measured at 1 K. Fitting was performed using the Gumbel distribution (2.18), showing good agreement with the experimental data.

$$P(I) = A \exp\left(\frac{\Delta I}{b} - \exp\left(\frac{\Delta I}{b}\right)\right) \tag{2.18}$$

with $\Delta I = I - I_s^{max}$, where I_s^{max} is the current with the highest probability for switching. The width of the curve is proportional to b. The Gumbel-distribution fit to the distribution of switching events is shown in Figure 2.4.

2.3. DC-SQUIDs

The Direct Current Superconducting Quantum Interference Device (DC-SQUID), called SQUID, is essentially a superconducting loop interrupted by two Josephson junctions, as shown in Figure 2.5. These devices show a dependence on the highest applicable zero-voltage bias current on an external magnetic field. As a result, SQUIDs can be used in magnetometry for measuring brain currents [39], building scanning SQUID microscopes [40], or investigating magnetic molecules[7].

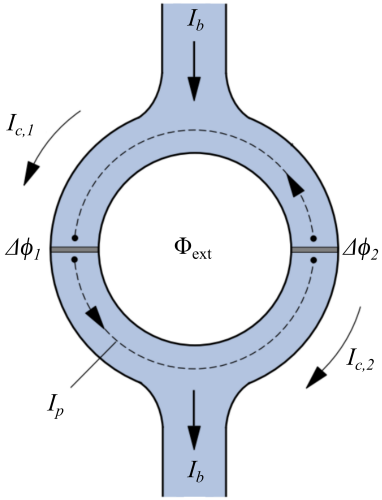

Figure 2.5. – A DC-SQUID consists of a superconducting loop interrupted by two Josephson junctions. Sourcing a bias current I_b through the loop creates a current through the junction, resulting in a change of the superconducting phase. The maximum applicable current before switching to the resistive state I_s depends on the junctions and the persistent current I_p. An external magnetic field creates magnetic flux Φ_{ext} inside the loop and changes I_p and therefore I_s.

The theoretical derivation for the SQUID properties is based on the highest applicable current in the non-resistive state, usually called critical current. The experimentally measurable property is the switching current, at which the transition to the resistive state happens. As both are expected to show similar behavior, both will be referred to as I_s. As both junctions are in series, the supercurrent through a SQUID is the sum of the currents passing through the junctions. For a symmetric SQUID consisting of two equal junctions, the biased supercurrent is

$$I_b = I_0(\sin\delta_1 + \sin\delta_2) \tag{2.19}$$

using the phase differences δ_1 and δ_2 across the junctions respectively. Applying a magnetic field H_z perpendicular to the SQUID plane induces a flux

$$\Phi_{ext} = \mu_0 H_z \cdot A, \tag{2.20}$$

through the area A of the SQUID loop. The flux quantization in a superconducting loop connects the two phases δ_1 and δ_2

$$\delta_1 - \delta_2 = \frac{2\pi\Phi_{ext}}{\Phi_0} + 2\pi n. \tag{2.21}$$

As a result, we get the supercurrent

$$I_b = 2I_0 \sin\left(\frac{\delta_1 + \delta_2}{2}\right) \cos\left(\frac{\pi\Phi_{ext}}{\Phi_0}\right). \tag{2.22}$$

As such, a SQUID behaves like a single Josephson junction with a modulating critical current modulating depending on the externally applied field and a phase difference of $(\delta_1 + \delta_2)/2$. As such, the critical current is

$$I_s(\Phi_{ext}) = 2I_0 \left|\cos\left(\frac{\pi\Phi_{ext}}{\Phi_0}\right)\right|. \tag{2.23}$$

This can be intuitively understood when considering the inductance $L(\delta) = L_J/cos(\delta)$ created by the junction using the Josephson inductance $L_J = \Phi/2\pi I_0$ [41]. The loop automatically contains an integer number of flux quanta for zero externally applied magnetic field, and I_s is $2I_0$. Therefore, increasing the magnetic field requires the generation of a persistent current I_p to mitigate the excess flux. This results in a reduction of the maximum bias current, resulting in the modulation.

An important deviation from this ideal case is the consideration of the inductance L_{Loop} around the loop. A finite inductance reduces the modulation but leaves the minimum pointed, as shown in Figure 2.6. With the same argument as for the modulation, for $L_{Loop} \neq 0$ as smaller I_p is required to satisfy the relation

$$\Phi = \Phi_{ext} + L_{Loop} I_p = n\Phi_0. \tag{2.24}$$

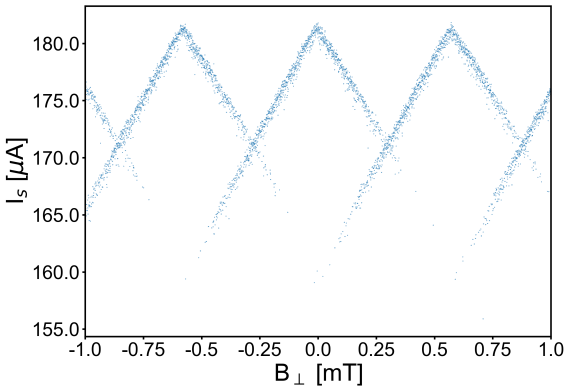

Figure 2.6. – Modulation of a highly inductive SQUID made out of niobium nitride measured at 1 K.

The relative modulation ΔI_c, being the difference between the maximum and minimum of the critical current for an inductive SQUID, is given by

$$\frac{\Delta I_s}{I_s^{max}} := \frac{I_s(\Phi = 0) - I_s(\Phi = 0.5)}{I_s(\Phi = 0)} = \frac{1}{1 + \beta_L} \tag{2.25}$$

using the screening factor

$$\beta_L = 2I_0 L_{Loop}/\Phi_0 = I_s^{max} L_{Loop}/\Phi_0 \tag{2.26}$$

as a measure of the loop inductance [42], furthermore, for large enough L_{loop} a sufficiently high I_p can change the fluxquanta penetrating the loop away from the case closest to Φ_{ext}. This results in a multivalued modulation of $I_s(\Phi)$ as shown in Figure 2.6.

3. Single Molecule Magnets

Applying magnetometry and electron paramagnetic resonance capabilities in this setup will be shown in Chapter 7 by analyzing a mononuclear lanthanide single-molecule magnet. A summary of the general properties of lanthanide complexes and the basic theoretical framework will be provided for a better understanding.

3.1. Spin Hamiltonian Formalism

For a detailed description, we must consider a magnetic center placed inside a molecular environment manipulated by DC and RF magnetic fields. The characteristic Hamiltonian can be written as:

$$\mathcal{H} = \mathcal{H}_0 + \mathcal{H}_{ee} + \mathcal{H}_{SO} + \mathcal{H}_{LF}. \tag{3.1}$$

Here,

$$\mathcal{H}_0 = \sum_k \left[\frac{1}{2m} \left(\vec{p}_k + e\vec{A} \right)^2 + g_e \mu_B \left(\nabla \times \vec{A} \right) \cdot \vec{s}_k - \frac{Z * e^2}{r_k} \right] \tag{3.2}$$

provides the sum of the hydrogen-like terms, which considers the hyperfine and Zeeman interaction through the magnetic potential $\vec{A}$. Furthermore, we take the interelectronic repulsion

$$\mathcal{H}_{ee} = \sum_{k<j} \frac{e^2}{r_{kl}}, \tag{3.3}$$

the spin-orbit coupling

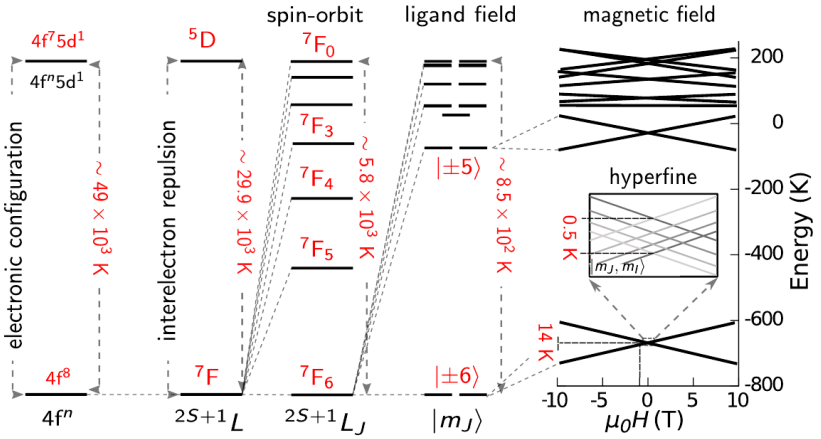

Figure 3.1. – schematic representation of the dominant intramolecular interactions in the $TbPc_2$ single molecule magnet. The $4f^8$ - $4f^7 5d^1$ transition can only be excited on energy scales above 49×10^3 K. The LS-coupling scheme separates the ground state ^7F from the first excited one, ^5D by 29.9 K due to electrostatic repulsion. Spin-orbit coupling splits the previously degenerate states characterized by, $S = 3$, $L = 6$ and a total angular momentum, $J = 0, 1, .., 6$ splitting the ground state $^7F_6$ from the first excited $^7F_5$ by ≈ 2.900 K. Interaction with the ligand ions further splits the $m_J = \pm 6$ ground state doublet from the first excited $m_J = \pm 5$ by >600 K. This ground doublet can be further split by the interaction with externally applied magnetic fields (14 K at 10 T applied field) and the nuclear spin. Adapted from [44].

$$\mathcal{H}_{SO} = \sum_k \xi(r_k)\vec{s}_k \cdot \vec{l}_k \tag{3.4}$$

and the ligand field interaction

$$\mathcal{H}_{LF} = -e \sum_k \int \frac{\rho(\vec{R})}{|\vec{R} - \vec{r}_i|} d\tau \tag{3.5}$$

into account.

As the Schrödinger equation, $H\psi = E\psi$ does not yield an analytical solution, a perturbative approach [43] was developed. This exploits that the interactions shown in Equation 3.1 operate on different energy scales, compare Figure 3.1.

For this, we start at solving $H_0\psi = E\psi$ with $\vec{A} = 0\,\mathrm{V/m}$. The resulting eigenfunctions can be written as a product of the hydrogen-like wavefunctions:

$$\psi(\vec{r}) = r^{-1}R_{nl}(r)Y_l^m(\theta,\phi) \tag{3.6}$$

where $R_{nl}(r)$ and $Y_l^m(\theta,\phi)$ provide the radial and angular dependence respectively. Here, the energy depends only on the quantum numbers n and l ($n = 4$ and $l = 3$ for the magnetic orbitals of the lanthanide ions). The lanthanides get characterized by the progressive filling of the 4f subshell with the electronic configuration $[\mathrm{Xe}]4\mathrm{f}^n6\mathrm{s}^2$. Characteristic features, such as the prevalence of the +3 oxidation state, 4f contraction of the atomic radius, unquenched orbital momentum, and easy ligand substitution, are grounded in the well-shielded nature of the magnetic electrons. For determining the magnetic anisotropy of Ln^{3+} complexes, the angular distribution of the 4f orbitals plays an important role [45].

As the inter-electronic interaction is dominant over spin-orbit interaction in lanthanide ions, the Russel-Saunders coupling scheme is applied. Here, the electrons get coupled together, forming a total spin angular momentum, S, while the orbital momenta couple together, forming the total orbital momentum, L. As a result, $\mathcal{H}_{ee}$ lifts the degeneracy of the $[\mathrm{Xe}]4\mathrm{f}^n$ leading to terms of the form, ${}^{2S+1}L$.

Here, the total angular momentum, J, takes $2L + 1$ (for $L > S$) or $2S + 1$ (for $S > L$) degenerate values : $J = |L - S|, ..., (L + S)$. this degeneracy gets broken by the spin-orbit interaction:

$$\mathcal{H}_{SO} = \lambda\vec{S}\cdot\vec{L} \tag{3.7}$$

As a result, states characterized by the same L, S and different J are split by:

$$E(S,L;J) = \lambda/2\,[J(J+1) - L(L+1) - S(S+1)] \tag{3.8}$$

and consecutive states separated by

$$\Delta E = E(S,L;J+1) - E(S,L;J) = \lambda J \tag{3.9}$$

with $\lambda = \pm\xi/2S$ being positive for $n < 7$ and negative for $n > 7$. As a result, the ground state is $|L - S|$ for Ln ions with less than a half-filled shell and $L + S$ when the shell is more than half-filled.

The total orbital momentum of the electronic ground state in a free Ln^{3+} ion can be obtained by following Hund's rules applied in the following order:

- The spin S has to be maximized.
- The angular momentum L has to be maximized.
- The total angular momentum is $|L - S|$ for $n < 7$ and $(L + S)$ for $n > 7$ with the terms represented by ${}^{2S+1}L_J$.

The large magnetic momentum resulting from the large total angular momentum in the second half of the lanthanide series explains the focus of research on these elements. Furthermore, the spin-orbit coupling leads to a significant separation between the ground state ${}^{2S+1}L_J$ and the first excited state ${}^{2S+1}L_{J+1}$, leading to a complete occupancy of the ground state at room temperature.

3.2. Ligand Field Interaction

As lanthanide single-molecule magnets embed the Ln^{3+} into a molecular environment, the effect on the coordinated ions gets usually discussed in the framework of the ligand field formalism. The ligand field Hamiltonian H_{LF} (Eq. 3.5) includes the electrostatic potential by the ligated ions. Furthermore, covalent effects have to be included, as this approximation is not sufficient for molecular complexes.

For the evaluation in the perturbative approach, the following matrix elements have to be calculated:

$$\langle \psi_l | \mathcal{H}_{LF} | \psi_k \rangle \tag{3.10}$$

The spherical nature of the $|\psi\rangle$ eigenstates promotes the expansion of the potential as spherical harmonics. Using,

$$\frac{1}{|\vec{r} - \vec{R}|} = \sum_{k=0}^{\infty} \frac{4\pi}{2k+1} \frac{r^k}{R^{k+1}} \sum_{q=-k}^{k} Y_k^q(\Theta, \Phi) Y_k^q(\theta, \phi) \tag{3.11}$$

where R, Θ, and Φ are spherical coordinates that correspond to the ligated ions, while r, θ, and ϕ describe the 4f electrons. as a result, the ligand field operator can be written as:

$$\mathcal{H}_{LF} = \sum_{k=0}^{\infty} \sum_{q=-k}^{k} r^k \left(\frac{4\pi}{2k+1} \int \frac{\rho(\vec{R}}{4\pi\epsilon_0 R^{k+1}} Y_k^q(\Theta,\Phi) d\tau \right) Y_k^q(\theta\phi). \tag{3.12}$$

Here, the ligand degrees of freedom can be separated from the ones describing the 4f electrons with the ligand field parameters

$$A_k^q = \frac{4\pi}{2k+1} \int \frac{\rho(\vec{R}}{4\pi\epsilon_0 R^{k+1}} Y_k^q(\Theta,\Phi) d\tau \tag{3.13}$$

Using the irreducible tensor formalism to express Y_k^q as a function of equivalent spin operators [43, 46] leads to

$$\mathcal{H}_{LF} = \sum_{k} \sum_{q=-k}^{k} \alpha_k (1-\sigma_k) A_k^q(r^k) O_k^q = \sum_{k} \sum_{q=-k}^{k} B_k^q O_k^q \tag{3.14}$$

with the equivalent Steven's operators O_k^q, the Steven's coefficients B_k^q, the proportionality constants between Y_k^q and O_k^q α_k, and the screening constants σ_k.

The Steven's operators are functions of J_z, J_+, and J_- as listed in [43, 46]. The order of the operator is represented by the index k, while the subscript q denotes the operator's rotational symmetry. Only even terms generate non-zero matrix elements.

The coupling between $\vec{J}$ and an externally applied magnetic field $\vec{H}$ gets represented by the Zeeman term

$$\mathcal{H}_Z = g_J \mu_B \mu_0 \vec{H} \cdot \vec{J} \tag{3.15}$$

with the Bohr magneton μ_B and

$$g_J = \frac{g_L\left[J(J+1)+L(L+1)-S(S+1)\right]+g_S\left[J(J+1)+S(S+1)-L(L+1)\right]}{2J(J+1)} \tag{3.16}$$

3.3. Transition Metal Ion Compounds

The power of the ligand field formalism can be demonstrated by considering transition metal ion compounds characterized by a quenched orbital angular momentum. Here, the Hamiltonian can be written using the spin degrees of freedom in the first approximation. Due to coupling the magnetic ions to the surrounding ligand field, the spin-orbit interaction can not be neglected even when it is only considered a second-order perturbation. Using the quadratic terms in Equation 3.14 in zero external field yields

$$\mathcal{H} = DS_z^2 + E(S_x^2 - S_y^2) \tag{3.17}$$

D and E being common notations of the Steven's coefficients $3B_2^0$ and B_2^2 respectively. A presence of an easy axis allows choosing the spin coordinate system to align with the z-axis resulting in D being negative and $|E| \ll |D|$. The first term of this Hamiltonian splits the states of the S multiple, identified by the quantum numbers $m = -S...S$, into maximum twofold degenerate states with $E(\pm m) = -|D|m^2$. As a result, this magnetic anisotropy constant is often referred to as zero Field splitting (ZFS).

As a result, the energy levels follow a parabola, as illustrated in Figure 3.2. The height of the parabola $U = |D|S^2$ is called the anisotropy barrier. As the two sides correspond to opposing orientations of the magnetic moment, the ZFS can be used to estimate the energy barrier for the orientation reversal.

The height of the barrier and the time scale of the experiment determine the blocking temperature T_B, below which reversal processes through phonons vanish due to lack of energy. In the case of the Mn_{12}-ac on an experimental time scale of 1 s this amounts to $T_B \approx 4\,\mathrm{K}$. The increase in blocking temperature poses an important goal in the research of SMMs [47–49], with the record currently residing at an anisotropy barrier of 1760 K and T_B of $\approx 60\,\mathrm{K}$ [50, 51]. The second term in the Hamiltonian 3.17 poses a strong influence

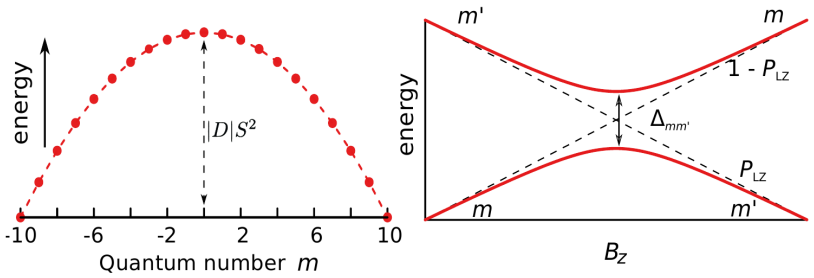

Figure 3.2. – left) Distribution of energy levels for a spin $S = 10$, subjected to the zero field splitting. right) Magnification of the energy level diagram around an avoided level crossing, where the levels characterized by the quantum numbers m and m' intersect. A spin in the m state has the probability P_{LZ} to tunnel to in the m' when continuously sweeping over this crossing. P_{LZ} increases for wider gaps $\Delta_{m,m'}$ and slower sweeping rates according to Equation 3.22. Adapted from [44].

on the low-temperature relaxation of magnetization (Section 3.5) and breaks the axial symmetry of the system.

3.4. Multi-Spin Hamiltonian

Despite numerous molecules, which contain a single magnetic ion [52], most SMMs contain multiple magnetic centers embedded in their organic shell, requiring an extension of the Hamiltonian.

A pair of spins coupled through exchange interaction can be described by [53]

$$\mathcal{H}_{exc} = \vec{S}_1 \hat{J}_{12} \vec{S}_2 \tag{3.18}$$

As the tensor $\hat{J}_{12}$ tends to be asymmetric, it often gets separated into the isotropic term $J_1 2\vec{S}_1 \cdot \vec{S}_2$ favoring parallel alignment, the anisotropic, symmetric term $\vec{S}_1 \hat{D}_{12} \vec{S}_2$ favoring alignment along a certain orientation in space , and the Dzyaloshinsky-Moriya term $\vec{d}_{12} \cdot (\vec{S}_1 \times \vec{S}_2)$ working towards a perpendicular alignment. In most cases, the isotropic term dominates, determining ferromagnetic or antiferromagnetic alignment depending on the sign.

For an arbitrary number of spins inside a system, the Hamiltonian gets generalized by combining the single ion anisotropies and pairwise exchange interactions resulting in

$$\mathcal{H} = \sum_i \vec{S} i \hat{D}_i \vec{S}_i + \sum_{i,j} \vec{S}_i \hat{J}_{i,j} \vec{S}_j \tag{3.19}$$

when only considering the quadratic term in the ligand field Hamiltonian. Even this simplification can not avoid the enormous set of parameters for clusters with high nuclearity. This can't be avoided, even when considering highly symmetric molecules.

3.5. Quantum Tunneling of Magnetization

The twofold degeneracy of the $\pm m$ generated by the ZFS gets lifted when applying an external magnetic field. On the other side, two levels denoted m and m' align, when the field

$$H_r^{m,m'} = \frac{|D|(m+m')}{g\mu_B\mu_0} \tag{3.20}$$

is applied along the magnetic principal axis. This degeneracy can be transformed into an avoided anti-level crossing by transverse terms of the ligand field Hamiltonian (Figure 3.2). The minimum energy difference $\Delta_{m,m'}$ is referenced as the tunnel splitting and plays a key role in characterizing quantum tunneling dynamics.

To theoretically determine tunnel splittings, different tools, such as path integral formalism [54, 55], perturbation theory [56, 57], and numerical methods, are available. While the latter allows the consideration of arbitrarily complex spin Hamiltonians, it leaves little intuition on the system's behavior. As a result, a combination of the techniques is preferred for both quantitative and qualitative analysis of SMMs.

An avoided level-crossing is formed when the base vectors corresponding to negative and positive spin projections start to mix into linear combinations to form the eigenvectors of the Hamiltonian. As a result, these states represent a non-zero probability of the magnetization of the spin to be on both sides of

the barrier. This is referenced as spin tunneling, where the spin is in quantum resonance between different spin states.

For an applied constant magnetic field tuned to an avoided level crossing, a spin initialized on one side of the well oscillates coherently between the mixed states. This happens at the characteristic angular frequency $\omega_T^{m,m'}$, which relates to the tunnel splitting by: $\Delta_{m,m'} = 2\hbar\omega_T^{m,m'}$. This is expected to happen around the field interval [53]

$$\delta H_r = \frac{\Delta_{m,m'}}{g\mu_B\mu_0|m - m'|}. \tag{3.21}$$

This is referred to as the bare tunnel width, which can be as small as 10^{-9} T. Besides the ideal case, the observed tunnel width of the resonance tends to get broadened by environmental interactions, which further hinder coherent oscillations.

3.6. Landau-Zener-Stückelberg (LZS) Model

Landau, Zener, and Stückelberg were the first to discuss the nonadiabatic transitions between the states of two-level systems [58–60]. As Landau and Stückelberg focused on two scattering atoms, the original work by Zener investigated the electronic states of a bi-atomic molecule. The derived solution for the time-dependent Schrödinger equation for a two-level system driven through resonance has been applied to many physical systems. It has become a valuable tool for studying tunnel transitions, as it was used to analyze spin tunneling in nanoparticles and clusters [61–64]. The tunneling probability P_{LZ} when crossing the resonance (Figure 3.2) can be calculated by

$$P_{LZ} = 1 - \exp\left(-\pi\omega_T \frac{\delta H_0}{\alpha}\right) \tag{3.22}$$

This model can be used to understand the hysteresis loops of SMMs qualitatively (Figure 3.3), which exhibit steps of fast relaxation with areas of constant magnetization in between. These steps happen at specific magnetic fields as discussed in Section 3.5, where transverse terms in the spin Hamiltonian mix states from both sides of the anisotropy barrier.

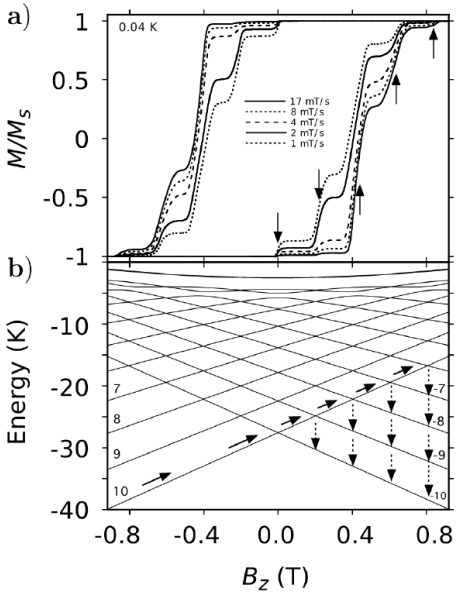

Figure 3.3. – a) shows hysteresis loops of a single crystal of Fe_8 performed at 40 mK and varying sweeping rates of the applied magnetic field. Prominent features are the distinct steps separated by plateaus of constant magnetization. The arrows indicated the steps caused by magnetic tunneling of magnetization, as highlighted in the Figure below. b) provides the corresponding Zeeman diagram of the $S = 10$ manifold of Fe_8 as a function of the magnetic field applied along the easy axis. The levels are labeled with the quantum numbers $m = -10, -9, ..., 10$ From bottom to top. Level crossings occur at equidistant field values of $\mu_0 H_z \approx n \cdot 0.22\,\mathrm{T}$ and $n = 0, 1, 2, ...$ Adapted from [44].

For large applied negative magnetic fields H_z and low temperatures, all molecules populate the $m = 10$ ground state (Figure 3.3). This is maintained when the H_z is ramped down to zero. When crossing the $\Delta_{10,-10}$ anti level crossing around $H_z \approx 0$, the spins can tunnel from $m = 10$ to $m' = -10$ at the Landau-Zener probability $P_{10,-10}$. The dependence of $P_{10,-10}$ on the sweeping rate (Equation 3.22) can be demonstrated, as slower sweeping rates show higher tunneling probabilities. This is indicated in the hysteresis loop with increasing step heights for the first steps [7, 65]. Further increasing H_Z puts the remaining molecules in the metastable $m = 10$ state. This can be escaped at the region around the $\Delta_{10,-9}$ splitting with the probability $P_{10,-9}$ by tunneling from the $m = 10$ to the $m' = -9$ state. From this excited $m' = -9$,

the molecules can relax under the emission of a phonon. This procedure continues when the applied field reaches the $\Delta_{10,-10+n}$; $(n = 2, 3, ...)$ regions until all remaining molecules are in the new ground state $m' = -10$. As a result, the magnetic moments of all molecules are reversed. Phonon emission can only change the molecule state by $\Delta m = \pm 1$ or $\Delta m \pm 2$, requiring a phonon cascade for higher applied fields.

An important constraint when applying the LZS model for quantitative analysis is the validity only for isolated spins, or it loses exactness. Environmental effects of both elastic (dephasing) and inelastic (relaxation and excitation) nature can cause deviations from the ideal coherent dynamics [6]. Agreement with LZS theory can be best achieved using large sweeping rates, so the time needed to cross the resonance is kept low, reducing the change in the local environmental field to a minimum. As the LZS doesn't include relaxation through phonons, these experiments should be conducted at very low temperatures and focus on ground-state tunneling.

Using these steps, the LZS model has been successfully applied to determine the tunnel splitting in molecular systems such as Fe_8 [66] and Mn_4[7]. The experimental difficulty of the reduced sensitivity due to the required fast sweeping rates can be overcome by repeatedly sweeping over the resonance. For this case, the probability of the spins to remain in the original state after n back-and-forth sweeps can be approximated by $(1 - 2nP_{LZ})$ for small changes in magnetization, with P_{LZ} given by Equation 3.22.

4. Low-Temperature Measurement Setup

The measurement setup is built around the Sionludi tabletop dilution cryostat built at the CNRS in Grenoble as explained in Section 4.1, to provide the cryogenic temperatures required. Those are needed for the SQUIDs to show the superconducting state and the SMMs to settle in their ground state. The complete overview of the setup is shown in Figure 4.1.

Atop of the cold plate of the cryostat, which reaches temperatures down to 20 mK, is a socket for the sample holder used for both thermalizing and connecting the DC- and RF-contacts to the outside. The sample holder is surrounded by a 3D vector coil setup to apply magnetic fields in all spatial directions.

Outside the cryostat are 3 GS-CS 10/20 high stability current sources by Georg Schmidt providing a stable current supply to the coil system. SQUID readout is performed by a self-built electronic developed at the CNRS in Grenoble. RF pulses are provided using the APULN40 frequency synthesizer by Anapico. The temperature inside the cryostat is monitored by the MMR3 module by Cryoconcept.

Time-sensitive operations are performed by the ADwin Gold II measurement unit from Jäger Computergesteuerte Messtechnik GmbH for real-time execution. The whole system is monitored and controlled by a desktop PC running the asynchronous acquisition program NanoQt developed at the CNRS in Grenoble.

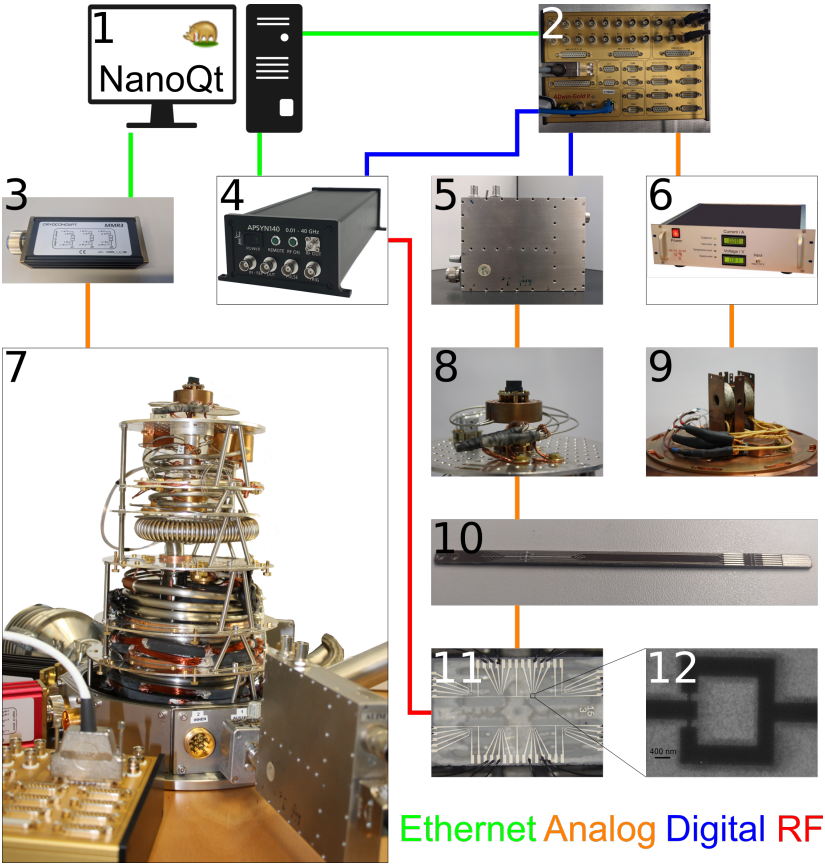

Figure 4.1. – Interaction between the devices used for measurements. This is performed by different kinds of communication, such as Ethernet (green), analog signals (orange), digital signals (blue) and RF pulses (red). Starting with a commercial desktop PC (1) running the asynchronous acquisition program NanoQt measurements scripts are sent to the ADwin Gold II measurement unit (2) and temperature is monitored by the MMR3 thermometry module (3). RF radiation can be applied by the APULN40 frequency synthesizer (4). The behavior of the SQUIDs (11, 12) placed on a sample holder (10) placed inside a socket (8) are measured by a dedicated SQUID electronic 5). Manipulation by magnetic field happens by a set of 3D vector coils (9) sourced by GS-CS 10/20 current sources (6).

4.1. The Sionludi Dilution Cryostat

To conduct measurements at temperatures down to 20 mK, a Sionludi tabletop dilution cryostat was used, developed, and built at the CNRS in Grenoble. Its working principle will be explained in this Section.

Cooling samples down to 4.2 K can be done by using liquid ^{4}He at ambient pressure [67]. Lower temperatures down to 1.5 K can be achieved by evaporating ^{4}He. The required latent heat for the transition from liquid to gaseous state is provided by the remaining liquid ^{4}He and leads to its cooling. In practice, this can be achieved, by pumping on the vessel containing the liquid ^{4}He to keep the pressure below the vapor pressure. Lower temperatures can be achieved by using ^{3}He. Its higher vapor pressure gives rise to higher cooling power and makes temperatures down to ≈ 0.3 K possible. For further cooling, a dilution cryostat can be used.

In this cryostat, a mixture of ^{3}He and ^{4}He is used. At temperatures below 0.87 K only a certain amount of ^{3}He can be dissolved in ^{4}He (≤ 67 %). Further ^{3}He will lead to a phase separation between a ^{3}He-rich and a ^{3}He-poor phase, as shown in Figure 4.2a.

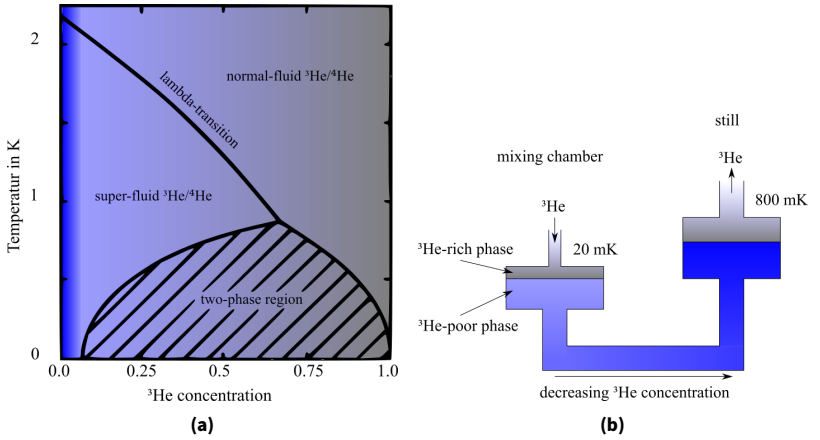

Figure 4.2. – Phase diagram for ^{3}He/^{4}He-mixtures. Above 0.87 K, ^{3}He can be diluted infinitely. Below 0.87 K the mixture separates into a lighter, ^{3}He-rich, and a heavier,^{3}He-poor, phase. Graph adapted from [67]. An application for this phase separation is the dilution cryostat. Extraction through pumping in the still creates a ^{3}He-gradient, which leads to ^{3}He-diffusion from the mixing chamber.

In an equilibrium state, both phases are well separated, and the lighter ^{3}He-rich phase floats on the heavier ^{3}He-poor phase. Extracting ^{3}He from the ^{3}He-poor phase allows ^{3}He from the rich phase to diffuse into the poor phase. For this transition, the so-called heat of the solution is provided by the mixture, similar to the diffusion of gas into a vacuum. This process takes place in the mixing chamber, which reaches the coldest temperature of 20 mK. The extraction of ^{3}He happens in a separate chamber, the still, which is connected to the bottom of the mixing chamber, as shown in Figure 4.2b. In the still, the mixture interfaces with the vacuum created by using a turbo molecular pump. Due to its high vapor pressure, mainly ^{3}He is evaporated in the still. The resulting osmotic pressure forces ^{3}He from the mixing chamber to the still, which provides a reduction of ^{3}He in the poor phase necessary for further diffusion.

For temperatures below 0.9 K the vapor pressure of ^{4}He goes to zero. On the other hand, increasing temperature leads to more evaporation of ^{3}He. For high cooling power, mainly ^{3}He should be evaporated. Therefore, the temperature of the still is kept $\approx$ 0.8 K. For continuous operation, new ^{3}He has to be provided with room temperature pumps without heating the system too much. The solution to this challenging task and the basic setup will be explained in the following section.

A picture of the cryostat used for my measurements is shown in Figure 4.3, while a schematic view is shown in Figure 4.4.

The cryostat is subdivided into seven stages, that have different temperatures. The top is formed by the so-called cold plate, which reaches temperatures down to 20 mK, while the bottom plate stays at room temperature. All stages are thermally decoupled through props made out of stainless steel and for isolation, vacuum and radiation shields at several stages are used.

When cooling down, the first stage is cooled down to 100 K with liquid nitrogen, which is provided by an external 11 l vessel. To reach the base temperature of 20 mK, two He circuits are used. The primary, closed circuit contains a ^{3}He/^{4}He-mixture, while the secondary circuit is supplied by a vessel next to the cryostat containing up to 100 l liquid ^{4}He (LHe). For cooling, the 5 K pot and the turbo condenser are filled with LHe, and pumping on the turbo condenser reduces the temperature down to 2 K, and evaporated ^{4}He gas leaves the cryostat through a counter flow exchanger and is collected by the recovery system. Passing the counter flow exchanger, the 4 K pot, and the turbo condenser, the mixture entering the primary circuit is precooled.

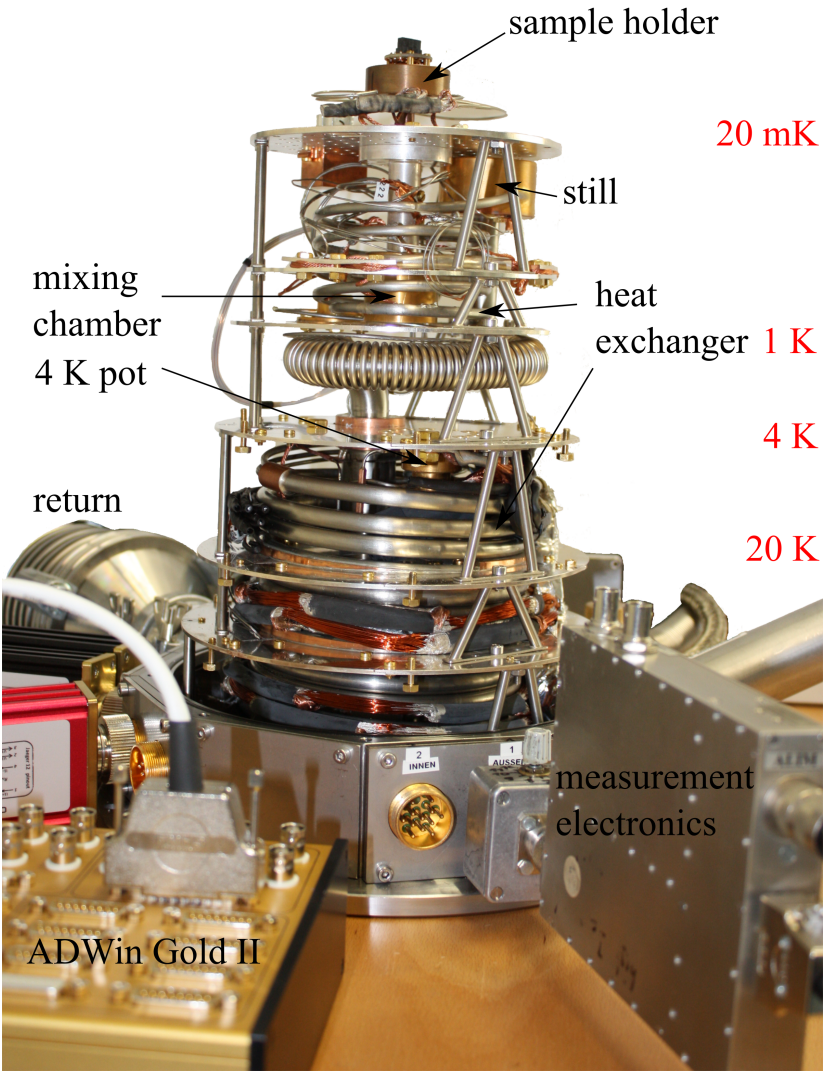

Figure 4.3. – Picture of the Sionludi dilution refrigerator and the measurement electronic used in the experiments presented in Chapters 5, 6 and 7.

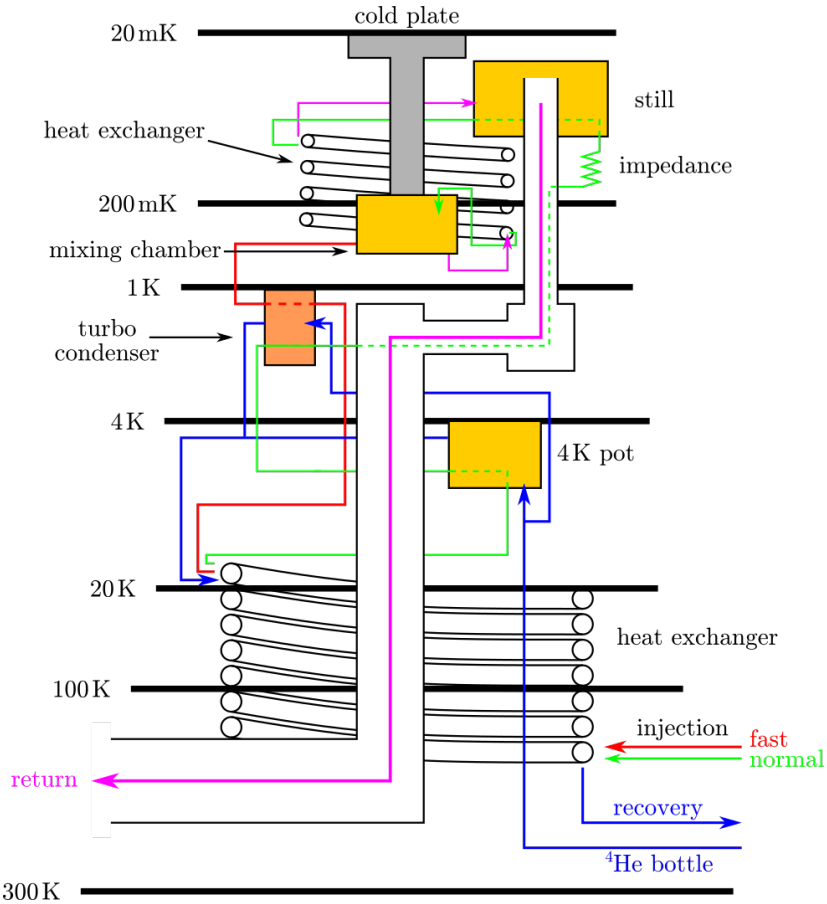

Figure 4.4. – Schematic view of the Sionludi dilution refrigerator. The primary cooling circuit consists of normal (green) and fast (red) injections. During operation, the normal injection is used for condensing the mixture in the mixing chamber, from where it is extracted via the still (violet). The fast injection is used during the pre-cooling process. The secondary cooling circuit circulates ^{4}He to precool the mixture. Adapted with changes from [67].

To reach the short cooldown times in the range of 3 h, which present a main advantage of the Sionludi, the gas injection is separated into the so-called fast injection and the normal injection. During cool down the larger diameter of the fast injection allows for faster circulation of gaseous mixture

for more efficient cooling, in addition to the normal injection, of the mixing chamber and the still and is used during precooling down to 4 K. After precooling, the mixing chamber is filled with liquefied mixture through the normal injection. Precooled mixture from the 4 K pot is further thermalized by cold ^{3}He gas evaporated in the still, before reaching an impedance. Here, further cooling is caused by the expansion of the gas due to the Joule-Thomson effect [67]. The mixture is further cooled down by thermalization in the still and a heat exchanger, before reaching the mixing chamber. The dilution, as described above starts when the mixing chamber reaches the phase separation temperature, which cools the cold plate to 20 mK. Further information about this brief overview can be found in [67].

4.2. Sample Holder Socket and 3D Vector Magnet

To mount the SQUIDs inside the cryostat a socket for the sample holder as shown in Figure 4.5a is used. The SQUIDs are glued to the chip carrier using a drop of PMMA resist for removability or a two-component epoxy adhesive for permanent fixation. Via bond pads, the SQUIDs are wire bonded to silver-covered copper lines on the carrier using a 25 µm Al wire. The sample holder is then inserted into the socket, which is thermally connected to the cold plate. The common ground line is connected to the mass of the cryostat, forming a common ground for the samples and all measurement electronics. 24 DC lines provide the possibility to connect up to 24 different SQUIDs. To apply magnetic fields, a 3D vector coil is placed around this shield avoiding any contact. The center is formed by a cylindrical coil around the sample holder, surrounded by two coil pairs, as shown in Figure 4.5b.

For thermalization, these coils are connected to the 4 K plate, and current is sourced through a chain of copper, HTc, and superconducting Nb-Ti leads from GS-Cs 10/20 current sources. A maximum current of 10 A can be applied to each coil in the plane of the SQUIDs and 5 A to the coil perpendicular to the SQUIDs. For the cylindrical coil which will be referred to as x-coil has a field strength of 140 mT/A, the coil pair in-plane of the SQUIDs, which will be referred to as y-coil has a field strength of 70 mT/A and the coil pair perpendicular to the SQUIDs, referred to as z-coil provides a field strength of 10 mT/A.

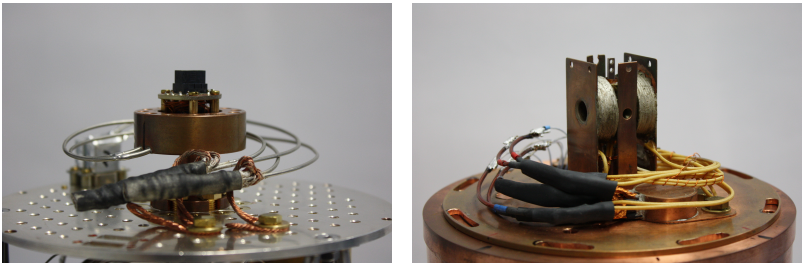

(a) (b)

Figure 4.5. – Picture 4.5a shows the sample holder, which is screwed to the cold plate and the connecting DC-Lines. In Picture 4.5b the 3D vector coils are shown, which are thermalized to the 4 K plate and connected to the current leads.

4.3. Quick Swap System

While the Sionludi dilution refrigerator is known for low cooldown times below 3 h, for an increased turnaround, a cold-swap system has been established. This allows the exchange of the sample holder without heating up the cryostat, except for the cold plate. Since no way to thermalize the sample holder at intermediate temperatures has been found yet, heating the cold plate can't be avoided. As the most time-consuming step, the recondensation is up-to-date the limiting factor resulting in requiring ≈ 45 min for the whole exchange.

As usual, a previous sample is still inside the cryostat, this one has to be extracted first. For this, the transfer arm gets mounted, and the load-lock evacuated to $<3 \times 10^{-5}$ mbar. As there is currently no automatic support for this procedure, the cryostat has to be set to manual mode. Afterward, the turbo pump gets shut down to avoid harming the pump through high flows of the evaporating mixture, and the ^{4}He-flow gets increased by 1 l/min to stabilize the system and avoid heating up of the coil system. Right before extracting, the shutters on the shield and the valve of the load lock get opened. Due to increased exposure to thermal radiation, the cold plate will rapidly heat up to 70 mK. Now, the transfer arm gets inserted, grabs the sample holder, and gets pulled out again. After closing the valve of the load lock and venting, the sample holder can get taken out.

For inserting the sample holder back inside, the above-mentioned steps have to be completed as well. In this case, it's crucial, that the turbo pump has spun down completely, as introducing a high thermal load of the sample holder to the cold plate causes strong heating and evaporation of the mixture. After taking out the transfer arm and closing the valve to the load lock, the standard cooldown procedure can be used to precool the mixing chamber to 4 K and recondense the mixture, until the base temperature of ≈ 30 mK is reached.

4.4. Magnetization Measurements

Hysteresis measurements on SMMs with μ-SQUIDs require the application of magnetic fields in every desired direction and the possibility to source current and detect superconducting switching at high frequencies. The centerpiece for these measurements is the ADwin Gold II measurement unit from Jäger Computergesteuerte Messtechnik GmbH. For communication, ADwin contains digital and analog in- and outputs in a range of −10 V to 10 V. The 16 bit resolution for input ports and 14 bit resolution for output ports provide voltage steps of 75 μV, and 305 μV, respectively. The input ports can be read out at 30 kHz. A real-time processor included in the ADwin provides synchronized control e.g., magnetic field and feedback loops. An additional Ethernet port provides communication with a PC.

As explained in Chapter 2 exceeding the critical current is indicated by a step in the I-V-characteristic. For I_s measurements, the current is ramped until a sudden increase in voltage is detected. To avoid heating during the normal conducting state, the current is shut down as fast as possible until superconductivity is restored. To increase frequency and resolution, the current is not ramped steadily but increases sharply to some constant value named plateau and after a short settling time starts the slope, as shown in Figure 4.6a.

When measuring a transition, the time since the beginning of the measurement is sent from the electronics to the ADwin with a resolution of 10 ns.

To get stable current sources in the mA an μA regime a voltage signal is generated. When placing a resistor in series to a SQUID and the resistor is chosen so large that the internal dynamic of the SQUID does not affect the

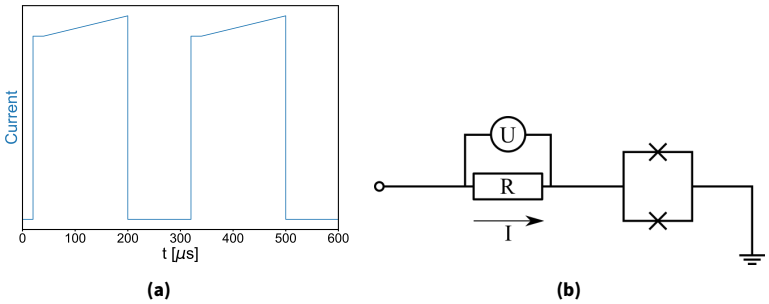

Figure 4.6. – Instead of sourcing a continuous ramp until the critical current I_s is reached, we ramp fast until the plateau value is reached and ramp from there, as shown in Figure 4.6a. When reaching I_s the current is shut down. As a result, the measurement electronic returns the time for which the current is ramped. 4.6b shows the scheme used for generating the bias current for the SQUID. For stable low-current sourcing, the main voltage drop happens at a resistor so large that the dynamic of the SQUID does not affect the current anymore.

current anymore a stable signal is generated, as shown in figure 4.6b. The plateau and the slope are set by a 16 bit and 12 bit integer respectively.

As applied RF radiation prevents meaningful I_s measurements as induced currents interact with the applied measurement pulse, continuous wave (CW) experiments require a different approach. Alternating RF pulses and I_s measurement pulses allow continuous readout, as shown in Figure 4.6a. Considering the relaxation times of the SMMs are in the range of up to seconds sufficiently large repetition rates in the range of 3 kHz to 10 kHz provide quasi CW behavior.

As shown in Chapter 2, the switching current is a periodic function of the applied external flux through the SQUID. Therefore, a particular I_s can be caused by multiple values of ϕ_{ext}. However, monitoring I_s provides a high sensitivity in detecting changes of flux in the range of $10^{-4}\phi_0$.

For hysteresis measurements, not the absolute value of ϕ_{ext} needs to be known, but only the change caused by the SMM. This provides the possibility to use a feedback loop, as shown in Figure 4.7.

For this, a certain I_s is chosen, named working point, as shown in Figure 4.8. When placing an SMM in the vicinity of a SQUID, any change in magnetization changes the flux through the SQUID due to the resulting magnetic field. Starting at the working point and measuring I_s, any change in ϕ_{ext} can be

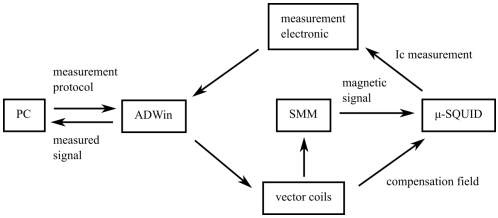

Figure 4.7. – Feedback loop used for μ-SQUID measurements.

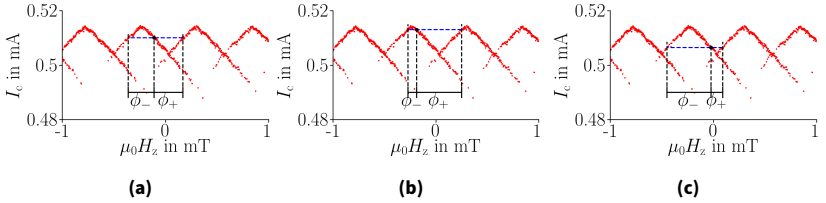

Figure 4.8. – Choice of working points in different situations. For possible flux changes in every direction, a working point in the middle of the modulation is chosen, as shown in Figure 4.8a. For mainly increasing or decreasing flux the working point is chosen higher or lower respectively to provide a higher measurement range, as shown in Figure 4.8b and 4.8c respectively.

detected. At the beginning of the measurement, the working point is chosen to be in the middle of the SQUID modulation to detect flux change in both directions, as shown in Figure 4.8a. Here a maximum change of flux $\Delta\phi_{\text{ext}} = \phi_0/2$ can be detected, denoted as ϕ_- for decreased and ϕ_+ for increased flux. After further measurements, it becomes clear if the signal tends to increase or decrease the flux through the loop, and the working point can be raised or lowered. This changes $\phi_\pm$ for a higher measurement range in one direction, as shown in Figure 4.8b and 4.8c.

Applying a compensation field using external coils the flux caused by the SMM can be compensated, which returns I_s to the working point. For the measurements, the compensation field is measured. The direction of this applied field determines the side of the modulation, where the feedback stabilizes and can be adjusted to the side which gives a more stable signal. On the other hand, these adjustments give less range to flux changes in the other directions, since passing an extremum destabilizes the feedback, which stabilizes again in the next period. Therefore these measurements are limited

in not knowing the exact amount of magnetization and all hysteresis curves have to be normalized to the magnetization in the saturated state $\pm M_s$.

5. High-temperature μ-SQUID measurements

While low-temperature magnetization measurements can be performed with many options such as Hall probe magnetometry [68–70], magnetometry based on magnetoresistance [71–73], spin-dependent tunneling with Coulomb blockade [74, 75], and spin-polarized scanning tunneling microscopy [76], SQUID magnetometry allows for one of the most detailed studies of the magnetization [11–19].

Compared to commercial SQUID magnetometer systems, the μ-SQUID technique has an improved sensitivity by ten orders of magnitude. This results from the direct coupling between the μ-SQUID loop and the magnetic sample. However, the operating temperature is limited by the critical temperature T_c of the μ-SQUID material. Here the NbN is used to fabricate μ-SQUIDs with a working temperature up to 12 K. As this covers the superconducting transition temperature of exciting materials such as Nb and FeSe, the fabricated μ-SQUIDs also allow for a detailed investigation of the magnetic properties of these materials across their whole working range. Nb is a type-II superconductor used for various superconducting applications, such as conducting high currents and the μ-SQUID technique. FeSe is the simplest iron-based superconductor. With its superconducting properties presumably related to its magnetism, its study provides ground for a deeper understanding of the relationship between superconductivity and magnetism.

To demonstrate the properties of these μ-SQUIDs , a stable temperature control has to be used. For this, a home-built temperature control system has been fabricated, as described in Appendix B. The design and fabrication processes are described in detail in Sections 5.1 and 5.2, respectively. The following Sections show different temperature dependencies used to demonstrate the applicability of these SQUIDs for magnetometry. At last, Section 5.6 shows the magnetization and relaxation measurement of a $Bi_{24}Mn_6$ single-molecule magnet, as a demonstration of the capabilities of this system.

5.1. Design of NbN-μ-SQUIDs

While the layout of the samples is based on the original design introduced by Prof. Wolfgang Wernsdorfer in his Ph.D. thesis [12] and my preceding master's thesis[77], important altercations have been performed to adapt to the respective applications. One 15 mm × 15 mm wafer is separated into 12 structures of 1.8 mm × 2.8 mm, which can be put onto the sample holder. All contacts can be performed via 150 μm × 50 μm bond pads arranged at the edges of the chip. Electrical connections to the sample holder are created via the wedge wire bonder by Westbond. From the bond pads, conduits run to the SQUIDs, which narrow down to 400 nm.

The SQUID is fabricated in a square shape with 2.4 μm outer side length and 1.6 μm on the inside. The increased width of the loop from 400 nm for Nb-μ-SQUIDs is to reduce kinetic inductance. Constrictions form the Josephson Junctions at both sides of the loop. This symmetric layout reduces the influence of the proximity effect during the e-beam lithography. The width of the constriction is designed at a width of 50 nm and a length of 50 nm. The other side of the loop is connected by a lead of 400 nm width to the ground, which is mostly formed by a common ground for all SQUIDs. The estimated effective surface area of the SQUID loop is 4 μm^2 resulting in a modulation period of $\Phi_0/4\,\mu m^2 \approx 0.5$ mT. For high working temperatures up to 12 K, the material niobium nitride (NbN) is chosen for its higher T_c of ≈ 17 K and established deposition techniques [78, 79]. Images of the chip are shown in Figure 5.1.

For proper allocation of the SQUIDs to the measurements, a coherent nomenclature has been established, if required, noted on the corresponding figures. The name (e.g., 16.11_2.10) locates the SQUID in the following order. The first number (16) reflects a continuous counter of the lithography round, reflecting different approaches and goals. The second number (11) reflects the chip cut from the wafer. Both numbers are noted on the chips to avoid any mix-up. If applicable, the third number (2) represents the subgroup on the chip, while the last (10) notes the exact SQUID of the subgroup. Numbering always goes from left to right and from top to bottom.

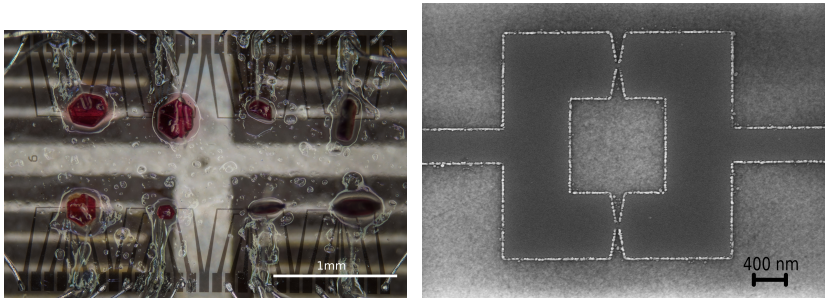

Figure 5.1. – Visualization of the sample design. a) shows the chip with a fully prepared sample. The top and bottom show the row of bondpads used to connect to the sample holder by wirebonds. From the bondpads, the connection leads narrow down and meet at the site of the SQUIDs. b) presents a closeup SEM image of a SQUID connected to the leads on the right and the left. The Josephson junction in the form of constrictions is at the top and the bottom.

5.2. Nanofabrication of µ-SQUIDs

All lithography steps are, if not noted otherwise, performed in the clean room facilities of the Nanostructure Service Laboratory (NSL) of the Center for Functional Nanostructures (CFN) at the Karlsruhe Institute of Technology (KIT). Fabricating these SQUIDs used for this thesis requires structuring Nb and NbN layers. The necessary steps contain thin film deposition, E-Beam Lithography (EBL), and Reactive Ion Etching (RIE). Figure 5.2 illustrates the structuring of the Nb and NbN layers, which will be discussed in the following Subsections.

5.2.1. Deposition

The Nb films are grown at the Néel Institute of the CNRS in Grenoble. The films are grown on sapphire at a thickness of 7 nm and covered under 2 nm of silicon (Si) to avoid oxidization of the surface [80]. We acknowledge Mr. Thierry Crozes for his help with the deposition of these films.

The NbN films are obtained at the Physikalisches Institut of the Karlsruhe Institute of Technology. The growth is done by RF magnetron sputtering from an Nb target in a high vacuum system with a base pressure below

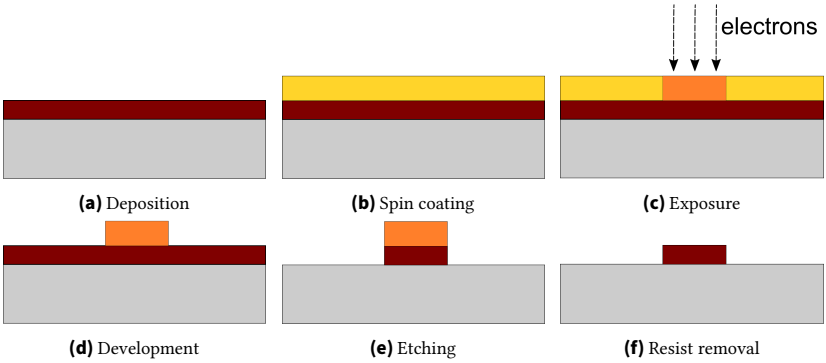

Figure 5.2. – Fabrication of μ-SQUIDs . a) On top of a sapphire wafer (grey), a thin superconducting layer (red) is grown. b) A thin homogeneous layer of resist (yellow) is applied by spin coating. c) The resist gets locally exposed to an e^--beam resulting in local polymerization of the resist (orange). d) Exposing the resist to a developing solution removes the unpolymerized parts leaving the exposed parts. e) Reactive Ion Etching removes the unprotected parts of the superconducting layer. f) Application of a solvent removes the residual resist, leaving only the nanostructured superconducting layer.

1×10^{-6} mbar and the substrate heated to 800 °C. 10 nm thick films were deposited on [0001]-oriented sapphire substrates at a growth rate of 0.1 nm/s. The total pressure of the Ar/N_2 gas mixture was adjusted to 7×10^{-3} mbar at an N_2 gas flow of 1.7 sccm. The film thickness of 10 nm is optimized to provide high robustness of the μ-SQUID to a magnetic field oriented in the plane of the film while maintaining a high superconducting transition temperature and critical magnetic field. The superconducting properties of the films were checked by 4-point resistivity measurements down to 2 K. The optimum NbN composition was derived from an almost temperature-independent behavior of the resistivity between room temperature and $T_c \approx 12$ K, where T_c was determined as the temperature where the resistance dropped to half the normal state resistance.

5.2.2. Electron Beam Lithography

To reach the high resolution required for SQUIDs, the structuring of the Nb and NbN is done by EBL. First, the Nb is structured using the negative resist ma-n 2401 by micro resist technology. Then, after cleaning the films with

acetone and IPA and drying them with pure nitrogen gas, the resist gets spin-coated. Before the electron beam exposure, the resist gets prebaked. After the exposure, the resist gets hard-baked before further processing.

For the structuring of NbN films into SQUIDs, the negative resist AR-N 7520.073 is used. After cleaning the films with acetone and IPA, resist is applied via spin coating. The exposure of the resist is followed by development and hard baking. The exact application parameters are listed in Appendix A.

5.2.3. Reactive Ion Etching

To use the finished etch mask, the sample is placed in the glass electrode in the RIE plasma etcher Etchlab 200 chamber from Sentech. For a clean process, the chamber is evacuated down to 5×10^{-5} mbar, and leftover process gases are removed. For etching, tetrafluoromethane CF_4 is used. Using a flow of 40 sccm, a chamber pressure of 2 Pa and 200 W of RF power, a plasma of ionized fluorine is created. These highly reactive radicals form a chemical compound with the Nb, which can be evaporated much easier than elemental Nb [81]. The high kinetic energy of the ionized plasma provides the required activation energy for evaporation. With this approach, the selectivity of chemical etching and the anisotropy of physical etching is combined with high etching rates [81]. The Nb films are etched for 30 s and the NbN film for 2×20 s. Afterward, the chamber is evacuated again to remove all residual process gas and vented with nitrogen. The residual resist can be removed by soaking the wafer at 90 °C in N-Ethyl-2-pyrrolidone (NEP) for several hours and cleaning in an ultrasonic bath for 5 min. For the structuring of NbN films into SQUIDs, the negative resist AR-N 7520.073 is used. After cleaning the films with acetone and IPA, resist is applied via spin coating. The exposure of the resist is followed by development and hard baking. The exact application parameters are listed in Appendix A.

5.2.4. Dicing

To separate the different chip from the original wafer, a DAD3350 wafer saw from DISCO is used. Next, a protective resist gets applied on top by spin coating to protect the structures from damage. Specific parameters are listed

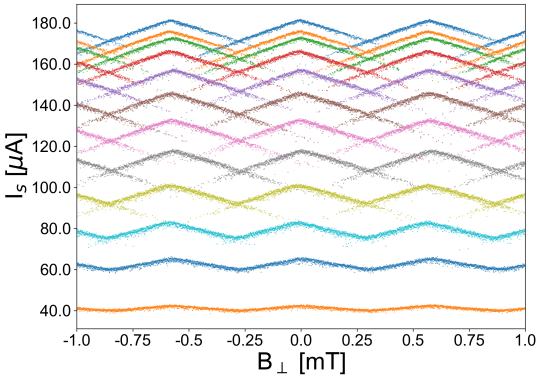

Figure 5.3. – Modulation of the critical current I_s vs out-of-plane magnetic field $B_\perp$ at various temperatures between 1 K (top) and 12 K (bottom) in 1 K steps.

in Appendix A. Finally, the protective layer can be dissolved in acetone after dicing, and after rinsing with IPA and drying, the chip is ready to be placed on the chip carrier.

5.3. Switching Current Modulation

A lot of information about the properties of a SQUID can be gained by analyzing the modulation of the switching current dependent on the applied external flux $\phi_{\mathbf{ext}}$. As discussed in Section 2.3, the shape can be strongly influenced by asymmetries in the critical current of the junctions and inductances and the presence of the inductance itself. A non-sinusoidal current-phase relation further changes the $I_s \propto |\cos(\pi\Phi_{ext}/\Phi_0)|$ behavior derived for the ideal case [20].

The measured modulation of an NbN μ-SQUID at increasing temperatures starting from 1 K up to 12 K is displayed in Figure 5.3. The modulation displays a period of about 0.5 mT as expected from the estimated loop area of 4 μm^2. Small deviations may occur from misalignment between the sample and the coil axis and inhomogeneities in the applied magnetic field, resulting in a reduced effective area of the SQUID loop. All curves show the same triangular

shape, which can be explained by considering the large inductance of the SQUID loop. Resulting from Equation 2.21 we get

$$\begin{aligned} 2\pi\left(\frac{\phi_{\text{ext}}}{\phi_0} - n\right) &= \delta_1 - \delta_2 + \frac{2\pi L_{\text{Loop}}}{\phi_0}\frac{I_1 - I_2}{2} \\ &= \delta_1 - \delta_2 + \beta_{\text{L}}\frac{I_1 - I_2}{I_{\text{c}}^{\text{max}}}, \end{aligned} \tag{5.1}$$

with n being an integer number. Using that for $(I_1 - I_2) \rightarrow 0$ we get $(\delta_1 - \delta_2) \rightarrow 0$, for large β_{L} the term $(\delta_1 - \delta_2)$ can be neglected [82]. Hence Equation 5.1, describing the modulation of the switching current, becomes independent of the current-phase-relation of the junctions:

$$I_2 = I_1 - \frac{2I_{\text{c}}^{\text{max}}}{\beta_{\text{L}}}\left(\frac{\phi_{\text{ext}}}{\phi_0} - n\right). \tag{5.2}$$

Using $I_{\text{c}} = max(I_1 + I_2)$ and $I_1, I_2 \leq I_0 = I_{\text{c}}^{\text{max}}/2$ results in

$$\frac{I_{\text{c}}}{I_{\text{c}}^{\text{max}}} = 1 - \frac{2}{\beta_{\text{L}}}\left(\frac{\phi_{\text{ext}}}{\phi_0} - n\right). \tag{5.3}$$

This shows that for large loop inductance, the switching current depends linearly in ϕ_{ext}/ϕ_0 with a slope of $\pm 2I_{\text{c}}^{\text{max}}/\beta_{\text{L}}$, which is equivalent to Equation 2.25 for large β_{L}.

Applying these results, we get an inductance 96.7 pH at base temperature and increasing at higher temperatures, which matches measurements on similar films [83].

Another essential feature is the multi-valued switching currents shown in Figure 5.3 resulting from switching from an excited state. Such switching events below the primary modulation curve are made possible by trapping several flux quanta inside the loop, which are not the closest to ϕ_{ext}. This corresponds to a phase particle trapped in an excited state of the SQUID potential with $\delta_1 \neq \delta_2$, as discussed in Section 2.3 [84]. This increases the circulating current, hence the reduced I_{s}. These excited states can be observed for $\beta_{\text{L}} > 1$, as present in these high inductance SQUIDs. This suggests that this signature for excited should be apparent in all modulation. Still, Figure

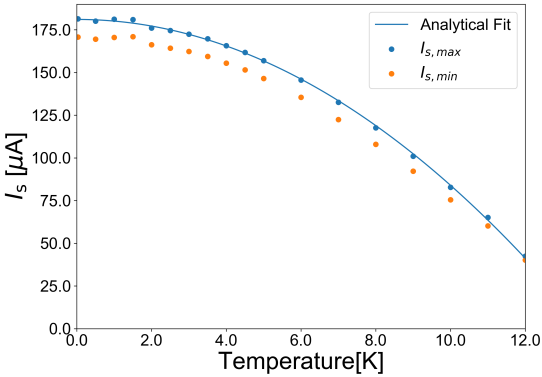

Figure 5.4. – Temperature dependence of maximum and minimum switching current shows parabolic behavior.

5.3 shows the disappearance above 10 K, while the inductance is expected to increase further . This might be explained by phase diffusion, where the particle, trapped in an excited state, undergoes phase slips before finally switching to the resistive state. Due to the phase slips, the particle relaxes to the ground state. This behavior is further indicated in the temperature dependence of the switching current distribution δI_s shown in Figure 5.6.

5.4. Switching Current Distribution

The performance for magnetization measurements is determined not only by the response to an applied magnetic field but for specific applied magnetic fields. To access the response without an applied magnetic field, repeated measurements of the switching current are performed and plotted in a histogram at several temperatures from 1 K to 12 K as shown in Figure 5.5.

A remarkable feature of the histogram is the asymmetric distribution. The theory of Kurkijärvi can model such distribution as a Gumbel distribution. By calculating the switching probability for the escape of the washboard potential by thermal excitation, we get the function

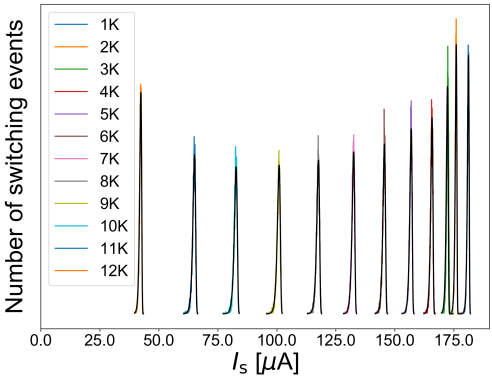

Figure 5.5. – Histograms of the switching current at various temperatures show good correspondence with the Gumbel distribution. This shows the applicability of the model of Kurkijärvi to describe the switching behavior of the NbN-μ-SQUIDs . A detailed version, measured at 1 K is shown in Figure 2.4

$$P(I) = A \exp\left(\frac{\Delta I}{b} - \exp\left(\frac{\Delta I}{b}\right)\right), \tag{5.4}$$

with $\Delta I = I - I_{\mathrm{sw}}^{\mathrm{max}}$, where $I_{\mathrm{sw}}^{\mathrm{max}}$ is the current with the highest probability for switching. The width of the curve is proportional to b. Indicated in black in Figure 5.5 are the fit of Equation 5.4 to the measured histograms. As the fit shows good correspondence with the measured data, this provides a basis to extract the most important parameters. As the natural distribution of the switching current due to the SQUID dynamics strongly influences the performance for magnetization measurements, the fitted distribution has been used to determine the Full-Width Half Maximum as the width of the switching current distribution δI_s. The temperature dependence of δI_{S} is shown in Figure 5.6.

Calculating the temperature dependence of δI_s from the model of Kurkijärvi, we get the expected dependence $\delta I_s \propto T^{1/b} I_{s,max}(T)^{1-1/b}$. We get three distinctive temperature ranges by applying this dependence to the measured data. First, for an intermediate temperature range between 2 K and 10 K, we observe a temperature dependence according to the applied model for thermally excited switching, where b depends on the potential of the specific

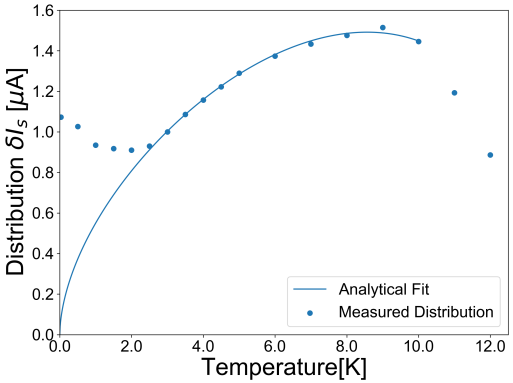

Figure 5.6. – Temperature dependence of the width (FWHM) δI_s of the switching current distribution I_s . The solid line shows a fit to the data according to the model of Kurkijärvi when considering thermal-activated quantum phase slips.

junction [33, 38]. For the NbN µ-SQUID , we obtain $b = 1.78$. Below 2 K, the data strongly deviate from the model (solid line), which is attributed to the increasing contribution of macroscopic quantum tunneling (QTM). Finally, starting from 10 K, δI_s drops stronger than predicted due to the strongly reduced I_s requiring more than one phase slip for heating the SQUID into the normal-conducting state [85]. This is in accordance with the disappearance of multi-valued switching in Figure 5.3 for high temperatures.

5.5. Sensitivity

As an indicator of performance, we compare these SQUIDs with other materials, such as niobium and aluminum. The sensitivity of the micro-SQUID is determined by δI_s divided by the slope of $dI_s/d\Phi_{ext}$ per $\sqrt{\text{Hz}}$. Figure 5.7 shows that for the NbN µ-SQUID, we obtain the best sensitivity of $5 \times 10^{-4}\,\Phi_0/\sqrt{\text{Hz}}$ at temperatures below 3 K. With increasing temperature, the modulation amplitude strongly decreases (Fig. 5.4) while the FWHM δI_s (Fig. 5.6) is almost unchanged, corresponding to a decrease of the sensitivity, in particular for temperatures above 10 K.

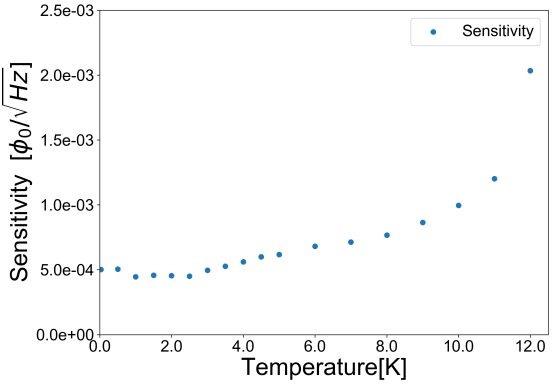

Figure 5.7. – Temperature dependence of the sensitivity in units of $\Phi_0/\sqrt{\text{Hz}}$.

This is in contrast to Al- and Nb-based SQUIDs with $1 \times 10^{-5}\,\Phi_0/\sqrt{\text{Hz}}$ and $1 \times 10^{-4}\,\Phi_0/\sqrt{\text{Hz}}$ respectively [20], strongly influenced by the high kinetic inductance.

5.6. Results for a $Bi_{24}Mn_6$ single molecular magnet

To demonstrate the potential and capabilities of the newly developed NbN μ-SQUID , we performed preliminary measurements on a single crystalline $Bi_{24}Mn_6$ SMM [86]. For recording an entire hysteresis loop of the magnetization, the sample was first thermalized at each temperature in zero magnetic fields, followed by magnetic saturation in -1.4 T. Subsequently, the magnetic field B in the plane of the SQUID was ramped to +1.4 T and back to -1.4 T. Figure 5.8 shows several hysteresis loops of M normalized to the signal M_S obtained in the magnetically saturated state at -1.4 T, for a sweep rate of 8 mT/s. While this SMM does not exhibit hysteresis at higher temperatures, the reduction in magnetization due to thermal excitation is still visible. This demonstrates that the available temperature range of the NbN-based micro-SQUID is a factor of two larger when compared to an Nb-based micro-SQUID which usually can be operated below 6 K.

Furthermore, it's possible to determine the barrier of the system. For this, the time-dependent relaxation of the magnetization for different temperatures

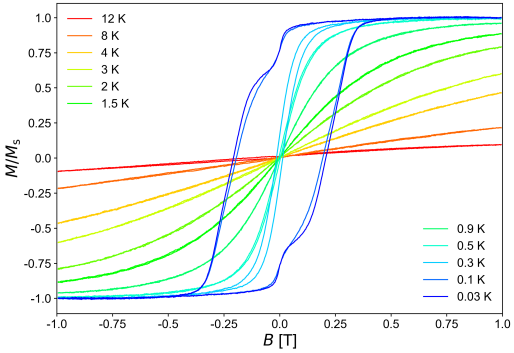

Figure 5.8. – Magnetic hysteresis loops M(B)/M_S of $Bi_{24}Mn_6$ single molecular magnets for different temperatures T. M_S is the signal at magnetic saturation at -1.4 T. The sweep rate of the field was 8 mT/s.

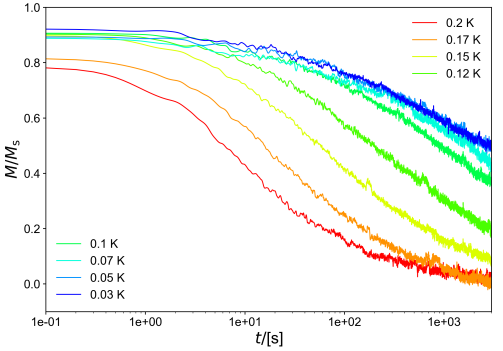

Figure 5.9. – Temporal relaxation of $Bi_{24}Mn_6$ SMM. At various temperatures, a crystal of SMMs gets saturated at 1.4 T applied magnetic field, and the magnetization relaxation at zero applied field gets measured over time.

is determined as shown in Figure 5.9. This is achieved with the same initialization protocol for saturation at -1.4 T as mentioned before. Afterward, the magnetic field is ramped down to zero with a sweep rate of 30 mT/s, and the decay of the magnetization signal was acquired over time.

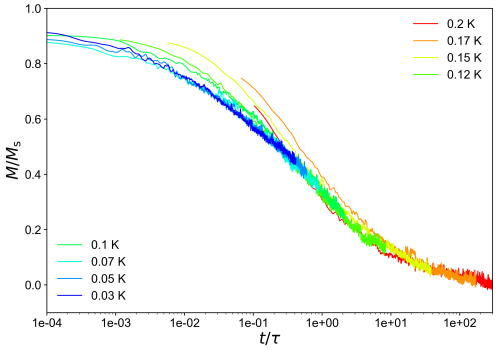

Figure 5.10. – Scaled temporal relaxation of $Bi_{24}Mn_6$ SMM to the temperature-dependent relaxation time. Scaling different relaxation curves to a single master curve allows the visualization of the relaxation behavior on different time scales and the determination of the temperature-dependent relaxation times.

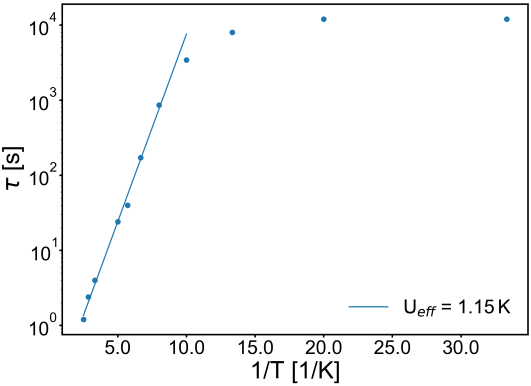

Figure 5.11. – Arrhenius plot of the temporal relaxation times at zero applied magnetic field of the $Bi_{24}Mn_6$ SMM. This allows the determination of the effective energy barrier $U_{eff} = 1.15\,\mathrm{K}$ as well as the saturation of the relaxation time around 1.2×10^4 s below 50 mK.

By aligning the different curves along a master curve, the temperature-dependent relaxation times can be extracted [87], as shown in Figure 5.10.

This shows that relaxation times below 100 mK are in the range of several hours. The extracted relaxation times can be visualized in an Arrhenius plot as shown in Figure 5.11. Using the dependence

$$\tau = \tau_0 \times \exp\left(U_{eff}/T\right) \tag{5.5}$$

allows the determination of the energy barrier $U_{eff} = 1.15\,\mathrm{K}$.

6. On-chip waveguide Design

From medical applications of NMR and EPR to cutting-edge research on quantum bits, the application of RF radiation plays an important role when manipulating quantum magnetic systems, such as the spin of electrons and nuclei. The development of different tools, such as electron paramagnetic resonance, spin echo spectroscopy, and selectively driving transition with circularly polarized radiation, provides the basis for a detailed investigation of these systems.

The demonstration of basic quantum algorithms demonstrates the suitability of single-molecule magnets based on the nuclear spin of rare earth ions. Using μ-SQUID magnetometry as an important tool to investigate these systems has been shown in Chapter 5.

To combine both concepts, this Chapter covers the development of a new setup to combine μ-SQUID magnetometry and RF radiation.

Improvements in the necessary periphery for guiding RF radiation and SQUID readout are given in Section 6.1 by the development of a new sample holder. Two sets of on-chip coplanar waveguides have been designed and fabricated for coupling RF radiation to the single molecule magnets, as covered in Sections 6.3 and 6.4. Characterization and the first applications of these designs are shown in Sections 6.5 to 6.8

6.1. RF-Sample Holder

A new sample holder is designed to integrate RF applications into the existing setup. As the sample holder has to fulfill a variety of essential properties, these must be considered during the design process. The sample holder needs to provide the necessary support for the chip, connectivity for 24 DC lines, two RF ports, and thermalization to the cold plate of the cryostat at mK

temperatures. Further desirable properties concern simplicity in fabrication and simple interconnectivity with the chip.

The layout of the PCB is designed using the open-source software KiCAD [88], enabling the design of multiple interconnecting layers.

As the inner diameter of the inner solenoid is 6 mm, this limits the outer diameter of the sample holder inside the solenoid to 4 mm, providing sufficient safety margin to correct for small misalignment errors during the installation process.

The choice of two RF connectors provides high flexibility in the choice of microwave application, allowing for reflective designs and transmissive or advanced structures providing local circular polarized radiation. The top layer features the corresponding CPW starting at the SMP connector at the bottom right to the mini-SMP at the top, both soldered to the PCB. The connectors get soldered to the PCB after the fabrication by placing them in the provided cutouts, applying solder paste, and heating the whole system in a reflow oven provided by the Electrical Workshop of the Physikalisches Institut at the Karlsruhe Institute of Technology. A cut-out for the chip provides precise placement and short connections helping with RF transmission. For even shorter connections, after processing milling, a hole close to the chip's height allows the chip's embedding in the sample holder and leveling the chip's surface with the adjacent conduits.

Thermalization and fixation to the cold plate of the cryostat are provided by two screwing holes to connect to the copper part of the socket.

The 24 DC lines to connect to the SQUIDs are spread over 2 layers below the surface, spread over two layers allowing for increased width and providing higher thermal conductivity and, therefore, better thermalization to the cold plate. The vicinity of the chip, shown in Figure 6.2b, shows the emergence of the DC lines using vias, small mechanically drilled and plated holes, providing conductivity between multiple layers. For easier bonding, these are capped, meaning filling with conducting material and closing at the top.

Chosen for its optimization for high-frequency operations and low losses, the material Rogers RO4350B is chosen [90]. The outer layers are designed with a matching thickness of 0.508 mm between the conducting layer 1/2 and 5/6, respectively. This symmetry is intended to inhibit bending due to unequal thermal shrinking by cooling to cryogenic temperatures. The inner layer between conducting layers 3/4 is 0.168 mm thick for a reduced

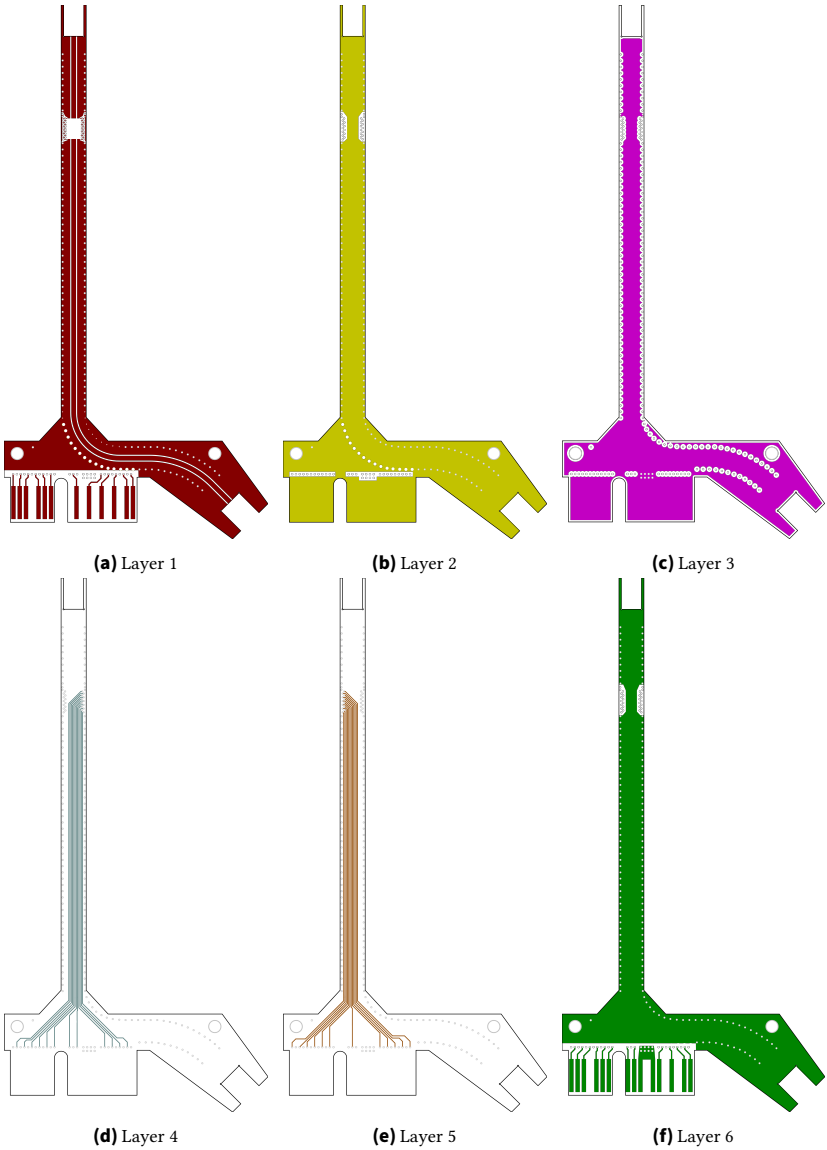

(a) Layer 1 **(b)** Layer 2 **(c)** Layer 3

(d) Layer 4 **(e)** Layer 5 **(f)** Layer 6

Figure 6.1. – Layers of the newly designed sample holder. The conducting copper parts are shown in color. The shape of the sample holder is outlined in black. Layers 1 and 6 feature 12 DC contact, fed through Layers 4 and 5 to the chip's site. Layers 2 and 3 act as electromagnetic shields between the CPW on top and the DC lines.

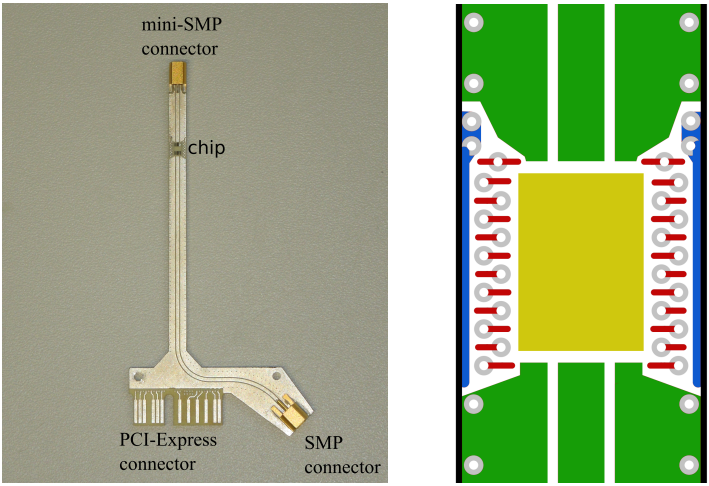

Figure 6.2. – a) Final sample holder, mini-SMP, and SMP connectors soldered to the PCB for RF connectivity. b) Magnified digital view of the area around the chip, showing the CPW (green), ground(blue), DC connections(red), place for the chip (yellow), and vias (grey circles). Adapted from [89].

thickness. This material further features excellent thermal stability of its dielectric constant $\varepsilon = 3.48$, maintaining the impedance match of the CPW even at low temperatures.

The conducting layers are applied by electrodeposition on both sides with a thickness of 17 µm [90]. These layers are combined by applying Megtron 6 between the conducting layers 2/3 and 4/5 as a sticking layer (called prepreg). To avoid oxidation of the surface, simplifying the wire bonding process, the outer layers are coated with 350 nm of silver. The choice of gold has been rejected due to the formation of an alloy at the interface known for its low thermal conductivity. The resulting thickness of 1.4 mm allows for a tight fit in the PCI-Express socket.

The CPW on top has a width of 0.76 mm and a gap spacing of 0.17 mm. Due to the proximity, the ground plane below has to be considered to form a grounded coplanar waveguide being a mix between a microstrip line and a coplanar waveguide. A detailed theoretical description can be found in [89, 91]. The vias along the waveguide are 1 mm apart to provide improved

thermal conductivity and electrical conductivity between conducting layers 1 and 2. This helps to suppress electromagnetic modes formed between the two planes by charge asymmetry [91]. To inhibit radiation from the board, vias should be spaced over the whole waveguide area with less than $\lambda/4$ distance[92]. This equates to1.25 mm at 40 GHz. As the 24 DC lines require significant amounts of space, only the edge of the PCB features vias spaced at 1 mm distance.

The manufacturer of the PCB is ITL circuits, based in Canada. 50 pieces of the PCB were made.

6.2. Design of RF-μ-SQUIDs

While most features of the SQUID design are discussed in Section 5.1, some optimizations for microwave applications were added. The leads of samples made for microwave applications have a constant width of 400 nm with a small distance of 400 nm in between to reduce coupling to the irradiated microwaves. The length of the constriction can be increased to 200 nm as kinetic inductance is less of a concern. On the other hand, the increased coherence length in Nb $\xi_0 \approx 39$ nm [93] requires longer constrictions to avoid increased switching currents.

As the material of choice, Niobium (Nb) is chosen for its working range from mK-temperatures up to 5 K. Furthermore, Nb shows great resilience against high in-plane magnetic fields, partially due to its low thickness of 7 nm. As the thickness is much smaller than the London penetration depth, the magnetic field can penetrate the superconducting film resulting in less expulsion of the magnetic field.

Nb films are grown at the Néel Institute of the CNRS in Grenoble and are provided by Thierry Crozes. The films are grown on sapphire at a thickness of 7 nm and covered under 3 nm of silicon (Si) to avoid oxidization of the surface [80].

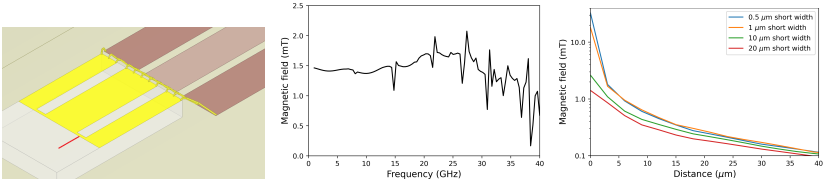

Figure 6.3. – Design of a reflecting on-chip waveguide. a) Design implementation consisting of an on-chip coplanar waveguide connected to the sample holder, where the inner conductor gets shorted to the ground. b) Broadband simulation of the magnetic RF field at the intended site of the SMM crystal for a short with 20 µm width. c) Decay of the strength of the magnetic RF field, which is inversely proportional to the distance to the short for different short widths. Adapted from [89].

6.3. Design of On-chip Coplanar Wave Guides

This Section is in collaboration with the Master's thesis of Daniel Schroller [89], supervised during this thesis.

For resonant excitations of SMMs, several critical requirements for the waveguide have to be met. For flexibility, the waveguide needs high transmission from DC to 40 GHz. This requires avoidance of resonances and impedance mismatches, which result in increased absorption and reflection. Furthermore, the magnetic RF field shall be focused at the site of the SMM for strong driving, while avoiding heating due to losses. Simplicity in processing and handling is preferred.

As a result, the choice fell on an on-chip coplanar waveguide. This represents a continuation of the coplanar waveguide on the sample holder connected via 20 µm aluminum bond wires. Two designs for the on-chip coplanar waveguide have been simulated, fabricated, and compared.

6.3.1. CPW in Reflection

For this design, the waveguide is terminated by shorting the inner conductor to the ground, as depicted in Figure 6.3a.

The width of the inner conductor is designed to be 0.68 mm with a 0.21 mm gap to the ground to allow for a distance of 0.7 mm between the measurement

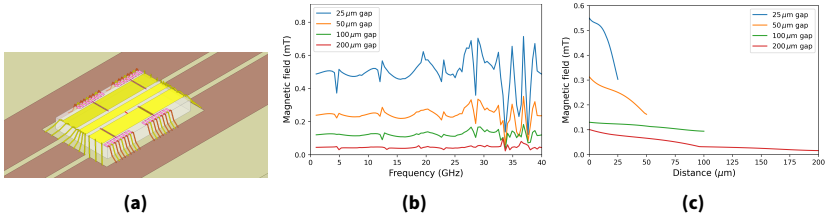

Figure 6.4. – Design of transmitting on-chip waveguide. a) Design implementation consisting of an on-chip waveguide connected to the sample holder. b) Broadband simulation of the magnetic RF field at the intended site of the SMM crystal for different gap sizes between the inner conductor and ground plane. c) Amplitude of the magnetic RF field across the gap for different widths. Adapted from [89].

sites. As the crystals are placed next to or above the short, this distance allows for separation to avoid interaction between the two samples. As shown in Figure 6.3b, the magnetic RF field strongly depends on the distance to the short, requiring proximity. As the magnitude for a 20 µm wide short already shows seems sound, further reduction in the width down to 1 µm would strongly increase the amplitude of the magnetic RF field. On the other hand, the increase in resistance would increase heating due to a stronger transformation of RF power to heat at the site of the crystal.

6.3.2. CPW in Transmission

This design explores the possibility of a coplanar waveguide in transmission, which will be terminated with an impedance-matched load at room temperature, as depicted in Figure 6.4a.

The SQUIDs will be placed in the gap between the inner conductor and the ground plane for high magnetic RF fields. As this design requires the crossing of the ground plane with the SQUID leads, the solution has been found in depositing an insulation layer in between, as will be explained in 6.4.1.

The broadband frequency sweep depicted in Figure 6.4b shows the high magnetic field over the broad range of frequencies. Above 33 GHz resonances start to appear due to the finite size of the ground plane.

6.3.3. Comparison

The main difference between both designs becomes clear when comparing the dependence of magnetic field strength on the distance to the waveguide. As the shorted version provides 1.2 mT at 1 µm distance to the 20 µm short, the transmission design only provides 0.55 mT even for the 25 µm gap. However, as the decrease in the field is inverse proportional to the distance for the shorted version, the transmission design shows lower dependence, nearly vanishing for the 100 µm gap.

Another concern is heating. To avoid thermal excitations of the SMMs, additional heating has to be avoided. As thinner cross-sections result in higher resistances and therefore stronger heating, this limits the applicable power, especially for the shorted version. The reduced thermal conductance of the waveguide reduces thermalization, resulting in higher local temperatures.

As the simulations don't provide a definitive answer over the best design, both have been fabricated and analyzed as detailed in Section 6.4 and 6.6.

For the fabrication of the coplanar waveguides, the material of choice is silver (Ag). Besides the issue of availability and cost Ag is chosen for its high conductivity and suppression of superconductivity. Of all available materials, Ag showed the best conductivity required to reduce heating when radiating microwaves at high powers. While superconducting materials such as the Niobium-Titanium (Nb-Ti) alloy are promising materials in this regard, the property of the repulsion of magnetic fields in the proximity of the SQUIDs is expected to create artifacts in the measurements as has been observed in the proximity of aluminum (Al) bond wires [12].

6.4. Nanofabrication of On-chip Coplanar Waveguides

As the fabrication of µ-SQUIDs using EBL is discussed in Section 5.2, the following Section focuses on fabricating the coplanar waveguides using optical lithography. All lithography parameters are listed in Appendix A.

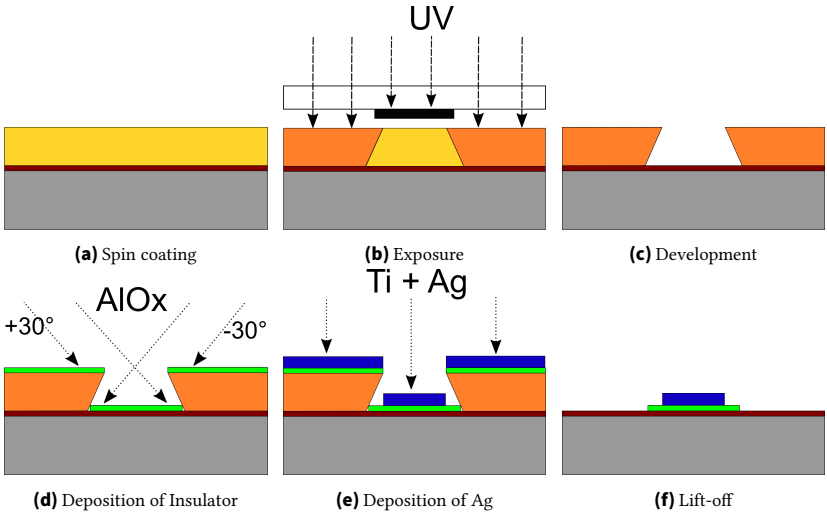

Figure 6.5. – Fabrication of coplanar waveguides. a) On top of a sapphire wafer (grey) and the μ-SQUIDs (red), a thin homogeneous layer of resist (yellow) is applied by spin coating. b) Selectively exposing the resist to UV radiation causes the resist to polymerize (orange). c) Exposing the resist to a developing solution removes the unpolymerized parts leaving the exposed parts. d) Depositing an AlO_x (green) diagonally at ± 30° creates an insulating layer, which extends below the undercut. e) Depositing the Ti adhesion layer and Ag (blue) orthogonally prevents any shortcut to the μ-SQUIDs . f) Dissolving the resist in acetone leaves the nanostructured coplanar waveguide.

6.4.1. Optical Lithography

Due to the expansive design of the coplanar waveguides used for coupling to microwaves, we resort to optical lithography. For this, the optical resist AZ 5214E by MicroChemicals is used in the negative mode. The spin coating is followed by exposure of the resist to 365 nm UV radiation in a hard contact mode. After a short thermal hardening step, a UV flood exposure turns the resist from the positive mode to the negative mode. After development, the wafer can be further processed. The exact application parameters are listed in Appendix A.

6.4.2. Deposition of ALO_x/Ag

Both AlO_x and Ag are deposited in the vapor deposition chamber of the PREVAC system installed at the Physikalisches Institut (PHI) at KIT. At pressures below 10^{-7} mbar, the mean-free path of kilometers allows the usage of electron beams to heat up and evaporate the desired materials inside a pyrolytic graphite crucible. Advantages of such a system compared to a directly heated vapor deposition system include the possibilities of higher final temperatures due to better thermal isolation and reduction of contamination from crucible material, especially when the crucible is water-cooled.

An advantage of the negative resist is the resulting edge profile, which gets a slight undercut during development, as indicated in Figure 6.5b. To place the SQUIDs in the gap of the coplanar waveguide, the connecting leads made out of superconducting Nb have to be placed below the ground planes of the waveguide made of normal conducting Ag. This requires them to be galvanically isolated from each other, which can be achieved using the shadow evaporation technique [94]. By evaporating aluminum oxide (AlO_x) under both $\pm 30^\circ$ it is possible to create an isolating layer that extends beyond the limits of the contour given by resist. For both angles, a layer of 25 nm is deposited. On top, a thin layer of 5 nm titanium (Ti) is deposited to increase the adhesion between the AlO_x and the Ag layer[95]. Since Ti has the ability to both form an ionic bond with the oxide ions at the surface of the AlO_x layer and a metallic bond with the Ag by forming an alloy at the interface, the resulting bond is stronger than the van-der-Waals bond without this adhesion layer. On top, a 100 nm layer of Ag gets deposited orthogonally.

6.4.3. Lift-off

After the deposition, the resist can be dissolved in warm acetone for the lift-off. After 7 min in the acetone, the beaker gets placed in an ultrasonic bath at maximum power for 1 min. For all resist, which doesn't get removed, small amounts of acetone can be pumped with a pipette. After rinsing with IPA and drying with nitrogen gas, the chip is ready for dicing.

6.5. External Heating

For a better understanding of the effect of the coplanar waveguide, hysteresis measurements on $[H_2NMe_2][Cr_7NiF_8(O_2CCMe_3)_{16}]$ are performed in the original setup[96]. This Cr_7Ni molecular ring is characterized by its collective $S = 1/2$. The appearance of hysteresis in the magnetization loops depicted in Figure 6.6a indicates the operation in the phonon-bottleneck regime at spin-phonon relaxation times in the s-range.

Using these hysteresis measurements, both equilibrium and out-of-equilibrium effects can be determined. For this, the effective spin temperature T_S can be calculated using the equation [43]

$$M(T_S)/M_S = \tanh\left(g\mu_B S\mu_0 H/k_B T_S\right), \tag{6.1}$$

using $S = 1/2$ and $g = 1.82$ as determined in [89]. A key feature to note is the adiabatic cooling, most prominent for high sweeping rates as shown in Figure 6.6b. This can be used for cooling to prepare quantum systems in the ground state. The difference between the equilibrium spin temperature and the bath temperature suggests opportunities for improvement in the thermalization as a cost-efficient alternative to reworking the cryostat when requiring lower temperatures, as well as the implementation of a radiation shield. This difference is even featured at higher bath temperatures, shown in Figure 6.6c. Changing to the new sample holder, as shown in Figure 6.6d while using SQUIDs in the old design, shows improved thermalization, as a slight difference in the design made for this setup provides more Nb conduits in the vicinity of the crystal providing better removal of excess heat. This becomes more evident when switching to the SQUID design for applying microwaves featuring long narrow conduits, as depicted in Figure 6.6e. The increase of the equilibrium spin temperature appears when the coplanar waveguide gets added with $T_{S,\,eq}$ exceeding 150 mK. This indicates that for temperature-sensitive measurements, further thermalization improvements must be made.

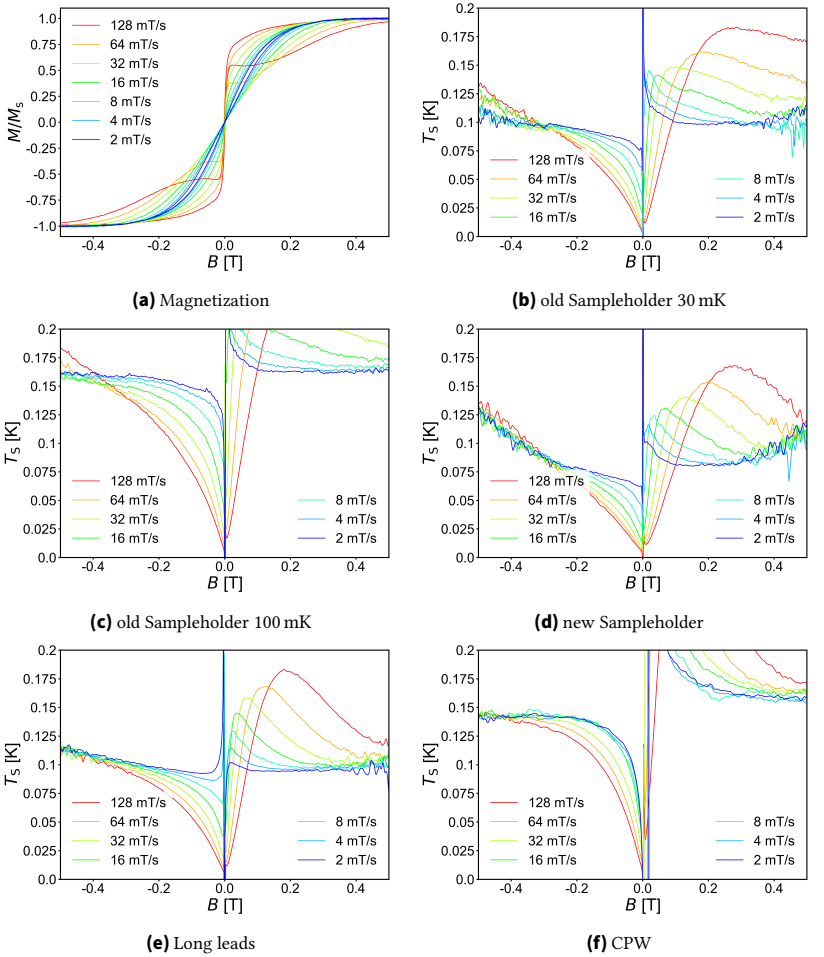

(a) Magnetization

(b) old Sampleholder 30 mK

(c) old Sampleholder 100 mK

(d) new Sampleholder

(e) Long leads

(f) CPW

Figure 6.6. – Spin temperature dependence on different Sample holder configurations. a) and b) show the magnetization curves and the spin temperatures during measurement with the original design used for μ-SQUID measurements as presented in Section 4.4. c) shows the spin temperature at an increased base temperature of 100 mK. d) presents the spin temperature using the newly designed sample holder as described in Section 6.1. e) provides the spin temperature for the new SQUID design featuring long and narrow leads. f) shows the increase in spin temperature due to the proximity to the coplanar waveguide.

6.6. Comparison of the Designs

Section 6.3.1 and 6.3.2 describe two different approaches to couple RF-radiation to the spin of an SMM. For this, a CPW working in transmission with a 10 µm wide gap and a CPW terminated with a 15 µm wide short are compared concerning the local magnetic field B_{ac} of the RF radiation. The procedure to extract this information from the resonance peaks is described in Section 7.4. Starting from the Rabi model , the probability P to find the system in the state $m_S = -1/2$ at the time t, after being in the state $m_S = +1/2$ at $t = 0$ is given by:

$$P = \pi(\gamma B_{ac}/2)^2 t\delta(\gamma B - \gamma) \tag{6.2}$$

in the limit of long times. The magnetic field acting on the molecule consists of the externally applied magnetic field B_0 and the local magnetic field B_L, for example, from other nearby molecules. Therefore the transition rate $\Gamma = \mathrm{d}P/\mathrm{t}$ gets integrated over the distribution of local fields $F(B_L)$, resulting in the spin-photon transition rate

$$\Gamma_L = \frac{\pi}{4}\gamma B_{ac}^2 F\left(B_L\right) \tag{6.3}$$

with $B_L = B_\nu - B_0$. As a result, the field dependence of the transition rate is determined by the distribution of the local fields, which can be fitted with a Gaussian function:

$$F(B_L) = \frac{1}{\sigma_L\sqrt{2\pi}} exp\left(-\frac{(B_0 - B_n u)^2}{2\sigma_L^2}\right). \tag{6.4}$$

The product

$$\Gamma\tau_S = \frac{1}{2}\left(\frac{M_{RF}(B_0)}{M_0(B_0)} - 1\right) \tag{6.5}$$

of the induced transition rates $\Gamma = \Gamma_L + \Gamma_0$ can be determined using the difference between the magnetization $M_{RF}(B_0)$ with RF radiation and the magnetization $M_0(B_0)$ without. The environmental heating effects get taken

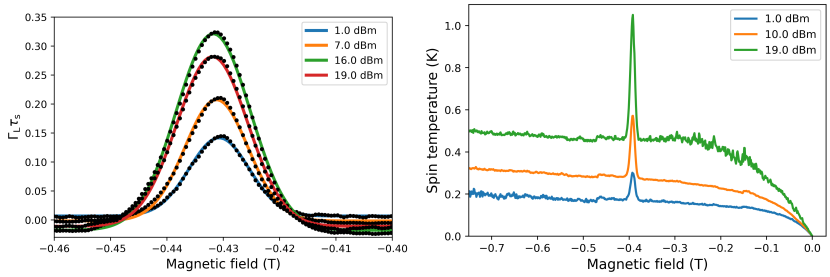

Figure 6.7. – a) Gaussian fits of $\Gamma_L\tau_S$ at a resonant frequency of 11 GHz. b) Spin temperature at 10 GHz. All measurements are performed with a pulse width of 1 µs every 300 µs.

in with Γ_0. $M_0(B_0)$ is determined by removing the effect of the peak with a strong gaussian filter as the narrow absorption dips are smoothed out. Relaxation measurements allow the determination of τ_S. After applying a strong exciting RF pulse, the resulting relaxation can be fitted with exponential decay and the characteristic relaxation time is determined to be 0.42 s

Figure 6.7a shows $\Gamma\tau_S$ determined by Equation 6.5 for different RF powers. For the highest powers of 16 dBm and 19 dBm, the peak height decreases as the characteristic spin-phonon relaxation time increases at higher powers .

Inserting Equation 6.5 into 6.3 provides the magnetic RF field. The fitted values are shown in Figure 6.8 for both designs. A constant relaxation times τ_S were assumed, resulting in some values of B_{ac} at high powers being smaller. At frequencies below 10 GHz, the CPW in transmission gives a higher magnetic RF field, while the behavior at frequencies is comparable.

6.7. Coil Calibration

An essential application of probing the Zeeman splitting Zeeman term $H_Z = g\mu_B\mathbf{BS}$ using EPR is the calibration of coils. For a system with a known g-value, we can derive the change in the resonance field δB_{res} for a given change of RF-frequency δf. As [77] suggested, a miscalibration of the 3D vector coils, especially between the x- and y-coil, will be further investigated. This is done using measurements of the $(Cr_7Ni)_2$diPy SMM. This dimer of

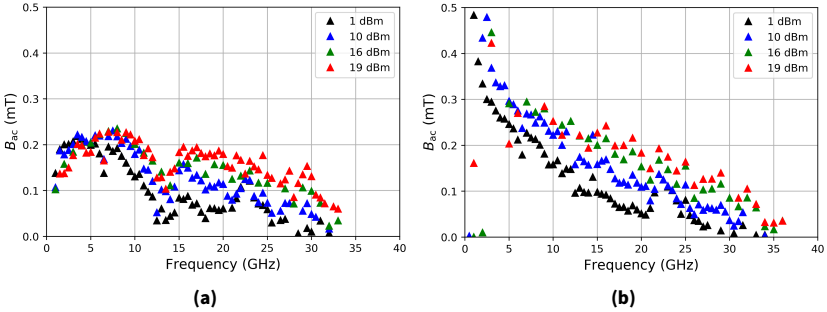

Figure 6.8. – Magnitude of the RF magnetic field B_{ac} for different powers and frequencies at a pulse width of1 µs every 300 µs. a) CPW terminated in a short circuit with a width of 15 µm. b) CPW in transmission, with a gap of 10 µm. Based on [89].

two coupled Cr_7Ni rings allows the comparison between the x- and y-coil. The measurement of the angular dependence of the EPR resonances is shown in Figure 6.9, which shows the difference between the irradiated loops and the background. The absorption peaks and dips are color-coded as white and black lines respectively against the orange background. The exact procedure to derive this data will be shown in Section 7.4.

6.8. Superconducting Coplanar Waveguide

Using the optical lithography approach outlined in Section 6.4, the minimum width of the fabricated short in the reflective CPW was determined to be 20 µm. As Figure 6.3c suggests, further decreasing this width is expected to boost the magnetic RF field. Therefore, a superconducting waveguide in the short circuit design with a width of the short of 1 µm was fabricated using E-beam lithography. For this approach, the waveguide was fabricated from the superconducting Nb-layer used for the SQUIDs as well, as this provided the easiest solution at hand as described in Section 5.2.

An important distinction can be found in the power dependence measurements of the resonance loops, as shown in Figure 6.10a. Starting at −2 dBm, the increasing power shows diminishing returns in absorption and strong heating of the sample. This can be attributed to exceeding the critical current at the superconducting short, providing a highly resistive element damping

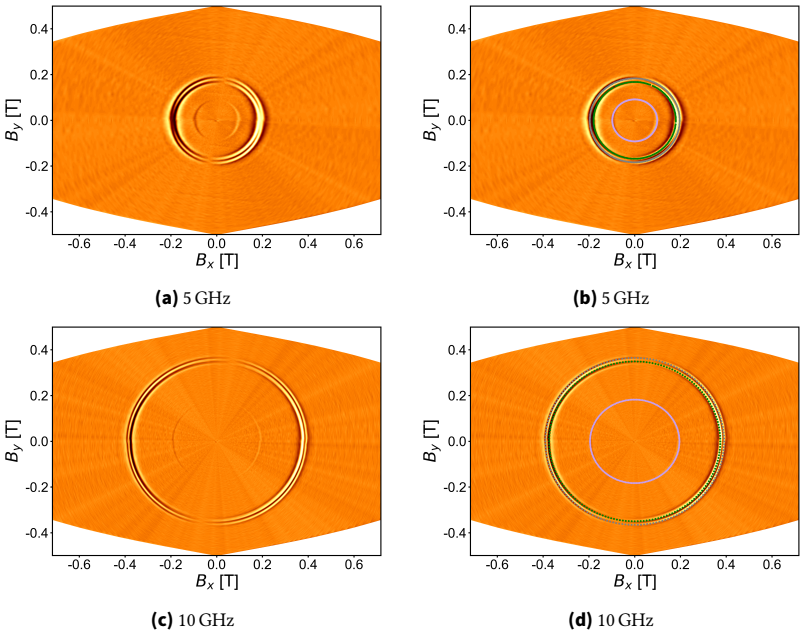

(a) 5 GHz **(b)** 5 GHz

(c) 10 GHz **(d)** 10 GHz

Figure 6.9. – Comparing the field maps of resonant absorption of the $[Cr_7Ni]_2$ SMM with simulated values shows only good correspondence when adjusting for the y-coil providing $\approx 7\%$ more magnetic field than the x-coil.

and heating the sample. This can be further investigated when analyzing different loops with the same average power but varying peak power, as shown in Figure 6.10b. The deposited energy averages out by varying the pulse width depending on the applied power, resulting in equal average powers. This shows two different behaviors. Low peak powers provide strong absorption while staying relatively cold. Above −2 dBm, the absorption decreases accompanied by an increase in spin temperature, visible by the washing out of the magnetization step.

This can be overcome by using a two-step process in which the second layer of superconducting material, such as Nb, gets deposited after the fabrication of the SQUIDs with an increased thickness providing higher current carrying capacity.

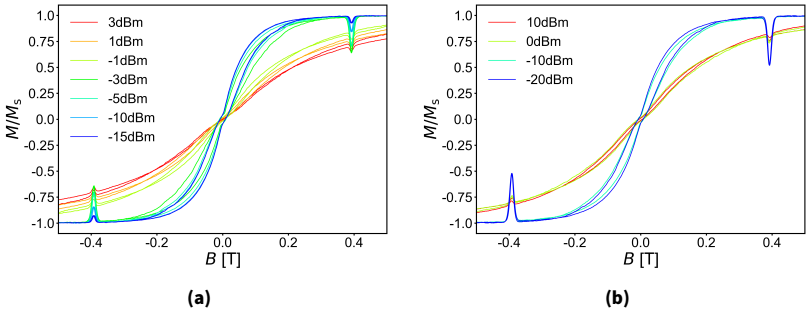

Figure 6.10. – Power dependence of the RF excitation of the Cr_7Ni single molecule magnet at 10 GHz. a) Varying the RF power at a constant pulse width of 100 ns every 300 µs, shows a transition at −2 dBm. b) Changing the pulse width depending on the power for constant average power shows the dependence on peak power instead of average power.

7. µSQUID-EPR on Gd^{3+} SMM

Ln^{3+} ions from the second half of the lanthanide series n>7 have been proven suitable for the synthesis of lanthanide-based single molecule magnets due to their large magnetic moment and large anisotropy [97]. During this thesis, a multitude of these systems has been analyzed. In contrast, Gd^{3+} (n = 7) based compounds are underrepresented in this area, as only a few examples have been reported in literature [98, 99]. In contrast, inorganic Gd^{3+} doped crystals were studied extensively to resolve the properties of S-state ion magnetic anisotropy [100, 101].

In contrast to most ions, Eu^{2+}, Mn^{2+}, Fe^{3+} and Gd^{3+} show zero average angular orbital momentum due to the half-filled magnetic shell. These S-state ions provide the ground to understand second-order, anisotropy-inducing effects, observable due to the $\langle L \rangle = 0$ property of these ions [102]. Furthermore, these were used for locally probing phase transitions, spin currents in conductors and semiconductors, site asymmetries, and orientation of the host lattice [103].

EPR techniques represent a crucial part of these studies, as they allow a detailed investigation of the properties of these ions embedded in various host lattices[43, 100]. These are predominantly operated at a fixed frequency while varying the magnetic field. Contrary, the zero field method is only scarcely used in the investigation of transition metals[104]. This importance is also represented in developing various EPR applications used in many branches of physical science [105].

This Chapter investigates diluted crystals containing Gd^{3+} based single molecule magnets using µ-SQUID-EPR. This will demonstrate the enormous capabilities stemming from this technique.

This will be demonstrated on the $^{160}Gd(tmhd)_3Phen$ variant (Fig. 7.1) showing a strongly distorted D_{4d} geometry, demonstrating the power of combining µ-SQUID and EPR techniques. The Gd^{3+} compound is chosen for its high spin

value (S = 7/2) and a ligand field splitting in the energy range below 40 GHz, providing a multitude of transitions below 1 T.

In this Chapter, the description of the $^{160}Gd(tmhd)_3Phen$ molecule with its chemical and structural characteristics will be provided, followed by the required theoretical tools for the analysis.

The experimental investigation of the $^{160}Gd(tmhd)_3Phen$ molecule starts with the μ-SQUID magnetometry measurements showing the necessity of further investigation tools provided by EPR. Introducing the EPR module allows for resonant excitation with electromagnetic radiation while measuring the magnetization, offering a more detailed probe of the system. The resulting measurement data successfully fit a set of spin Hamiltonian parameters.

7.1. Synthesis and Chemical Structure

For this study, a $^{160}Gd(tmhd)_3Phen$ complex was chosen as the subject of the study. The lanthanide complex is composed of an isotopically enriched Gd-containing source containing the ^{160}Gd isotope with 98.3 % enrichment. To minimize the complexity of the system and solely probe the crystal field effects in the SMM without hyperfine contributions, the ^{160}Gd source was chosen with $I = 0$. As expected by Hund's rules, the partially filled atomic shell of the Gd^{3+} ion is the half-filled 4f shell resulting in a total Spin $S = 7/2$ as the electronic state. The complex was obtained by reacting a mixture of $^{160}Gd(tmhd)_3 \cdot (H_2O)_2$ (tmhd = tris(tetramethylheptanedionato)) and phenantroline (Phen) in a 1:1 ratio in in absolute ethanol for 24 h. The obtained precipitate was successively crystallized from a mixture of ethanol and dichloromethane. Single crystal X-ray analysis showed the crystals to be the $^{160}Gd(tmhd)_3Phen$ complex (Figure 7.1). Two symmetrically related molecules are found to reside in the triclinic ($\overline{P}1$) unit cell. On the metal side, each metal ion possesses a N_2O_6 coordination geometry formed by six oxygen atoms from the tmhd groups and two nitrogen atoms of the Phen. The Gd-O distances range between 2.2994 Å to 2.3767 Å, whilst the Gd-N distances in both cases are longer, with values ranging from 2.6110 Å to 2.6151 Å. The coordination geometry around the gadolinium ions can be best described as a square antiprism with a Continuous Shape Measure (CShM) of 0.610 (Figure 7.1). Substitution of the $^{160}Gd(tmhd)_3 \cdot (H_2O)_2$ by $Y(tmhd)_2 \cdot (H_2O)_2$ lanthanide source yields the diamagnetic $Y(tmhd)_3Phen$ analog. Single crystal studies show the $Y(tmhd)_3Phen$

complex to be isomorphous with ^{160}Gd(tmhd)$_3$Phen analog. The diamagnetic Y(tmhd)$_3$Phen complex allows the magnetic dilution of the ^{160}Gd(tmhd)$_3$Phen complex.

All μSQUID-EPR measurements herein described were performed on single crystals of the complex with crystal sizes ranging from 10 μm to 50 μm. The ^{160}Gd(tmhd)$_3$Phen molecules were embedded in a Y(tmhd)$_3$Phen matrix with a 5 % content of ^{160}Gd(tmhd)$_3$Phen . As exchanging the Gd^{3+} ion in the Y^{3+} results in the same chemical structure, the diamagnetic Y^{3+} provides a noninteracting environment for the ^{160}Gd(tmhd)$_3$Phen molecules, while preserving the single crystalline structure of the samples. Due to this spatial separation of the ^{160}Gd(tmhd)$_3$Phen molecules, intermolecular interactions will be neglected in further discussions.

7.2. Spin System

The Gd^{3+} ion at the center of the ^{160}Gd(tmhd)$_3$Phen SMM is characterized by the [Xe]4f^4 electronic configuration. In the Russel-Saunders coupling scheme, this leads to the $^8S_{7/2}$ ground state separated by more than 30×10^3 cm^{-1} from the first excited multiplet ^{6}P. The degeneracy of such an isotropic ground state can only be lifted by an odd perturbation, for example, the coupling to an external magnetic field through the linear Zeeman term $H_Z = g\mu_B \vec{B}\vec{S}$ using the Bohr magneton μ_B and the gyromagnetic ratio $g \approx 2$ for the free electron.

When taking deviations from this pure $^8S_{7/2}$ into account and including a small admixture of the first excited ^{6}P, the resulting ground state can be expressed as:

$$\sqrt{(1-\alpha^2)}^8 S_{7/2} + \alpha^6 P_{7/2} + \ldots \tag{7.1}$$

with the corresponding g-value:

$$g = \left(1-\alpha^2\right) g\left({}^8S_{7/2}\right) + \alpha^2 g\left({}^6P_{7/2}\right) + \ldots \tag{7.2}$$

with α being in the range of 10^{-3}.

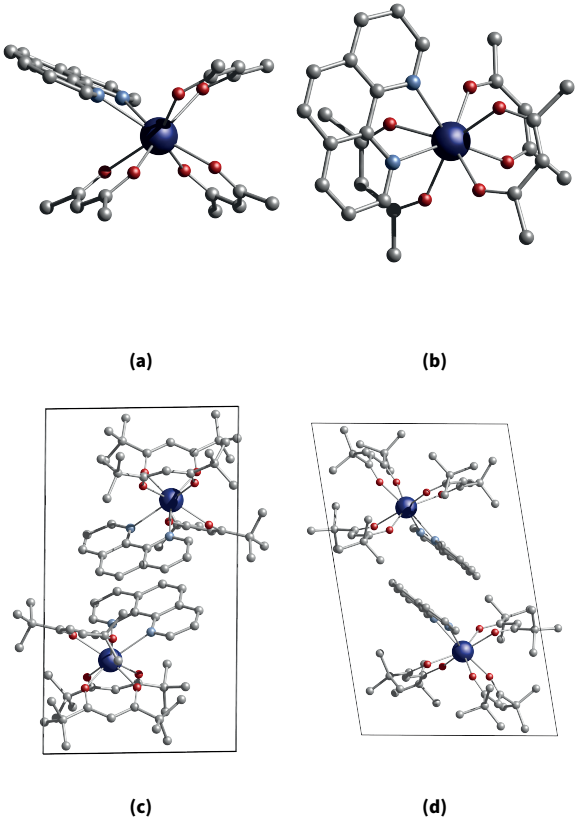

Figure 7.1. – a) Side view and b) top view $^{160}Gd(tmhd)_3Phen$ molecule (Me groups have been omitted for clarity). c) and d) show the unit cell of $^{160}Gd(tmhd)_3Phen$ with two molecules in the unit cell. Hydrogen atoms have been removed for clarity. (Colour code: Gd, dark blue; O, red; N, cyan; C, grey).

The resulting ligand field splitting due to the spin-orbit admixture in the ground state is around two orders of magnitude lower than in $\langle J \rangle \neq 0$ lanthanide molecular magnets. More details about anisotropy introducing interactions in S-state ions can be found in [102].

The influence of the ligand field will be modeled through the equivalent Steven's operator formalism as described in Section 3.2

$$H_{LF} = \sum_{n=1}^{3} B_0^{2n} O_0^{2n} + B_2^2 O_2^2 \tag{7.3}$$

with O_k^q being the Steven's operators [43] and B_k^q being the ligand field parameters.

While this provides a multitude of parameters, which must be considered, the required parameters can be narrowed due to various limitations. First, to account for time-reversal symmetry, only even terms must be considered, as they are invariant.

The resulting Hamiltonian for the ^{160}Gd(tmhd)$_3$Phen is the sum of the Zeeman and ligand field interaction:

$$H = g\mu_B BS + \sum_{n=0}^{3} B_0^{2n} O_0^{2n} + B_2^2 O_2^2. \tag{7.4}$$

Using only this basic set of ligand field parameters, we receive distinguished directions for the spin system's easy, medium, and hard axes. To relate this molecule frame with the laboratory frame based on the SQUIDs, we introduce the following relationship based on the Euler angles [106]. First, we align the x-y-plane of the laboratory frame with the x-z-plane of the spin system, as we often want to apply the magnetic field along the easy axis. The angle φrepresents a rotation of the molecule frame around its y-axis, as the easy axis can't always be aligned with the x-axis of the laboratory frame. This angle can be experimentally determined using the transverse field method [107]. The angle γ_1 represents a rotation around the x-axis of the spin system frame and the tilt out of the laboratory x-y-plane of the easy axis. Finally, γ_2 is the angle of a final rotation around the easy axis, representing a tilt of the spin system x-axis out of the laboratory x-y-plane. Figure 7.2 shows a visual representation of this relationship.

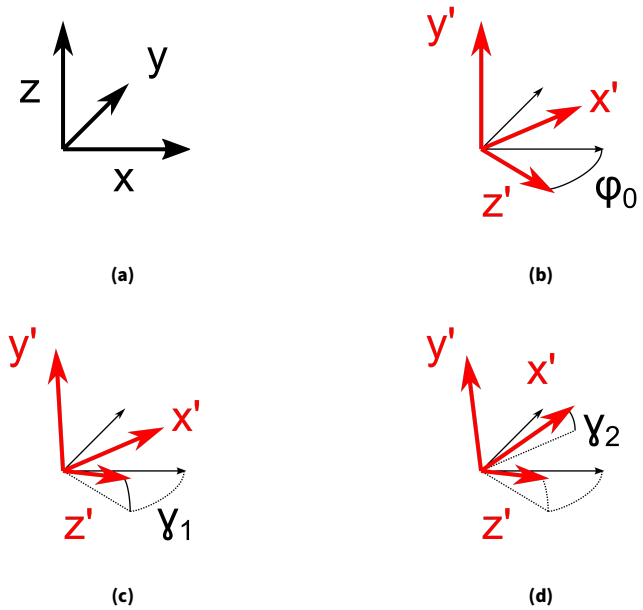

Figure 7.2. – Transformation between the Lab frame (black) and the frame of the spin system (red). The angle φ_0 represents the projection of the easy axis onto the plane of the applied magnetic field (x-y-plane). The angles γ_1 and γ_2 provide the tilt of the easy-axis out of this plane, as well as the tilt of the medium axis (x') out of this plane.

7.3. Magnetization Measurement

The first analysis of the $^{160}Gd(tmhd)_3Phen$ crystal is performed by magnetic hysteresis measurements using the μSQUID-technique, as described in Section 4.4. For this, the crystal is placed near an array of μ-SQUIDs fixed by Apiezon N vacuum grease. The crystal's placement and orientation are performed using a wire bonder by Westbond as a micromanipulator. For the measurement, the crystal is cooled down to mK-temperatures using the Sionludi dilution cryostat. A magnetic field can be applied in any direction using the 3D vector coil system, allowing the determination of the projection of the easy axis onto the SQUID-plane using the transverse field method [107].

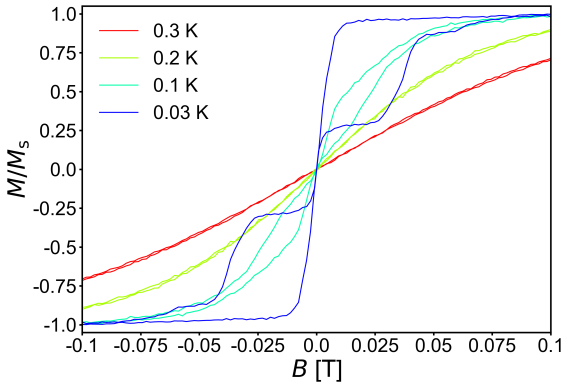

Figure 7.3. – Temperature dependence of the magnetic hysteresis of a single crystal of the ^{160}Gd(tmhd)$_3$Phen single-molecule magnet.

Figure 7.3 shows the temperature dependence of the magnetic hysteresis at a fixed magnetic field sweeping rate of 128 mT/s. This indicates the transition from an open hysteresis loop to superparamagnetic behavior at a blocking temperature below 0.2 K, as phonons provide sufficient energy to enable over-barrier relaxation.

A key feature of the hysteresis loops is the big step at zero field due to the quantum tunneling of magnetization. As the ground state of the Gd^{3+} ion features a half-integer spin $S = 7/2$, Kramer's theorem requires the degeneracy of the ground state doublet $m = \pm 7/2$. It is assumed that environmental spins, both electronic and nuclear origin, break Kramer's degeneracy, enabling relaxation through QTM.

While these studies provide a crude insight into the energy spectrum of these molecules, the details vary enormously depending on the amount of visible QTM, indicating avoided level crossings in the underlying Zeeman diagram. This can be seen as Figure 7.3 shows only a fraction of transitions compared to measurements presented for the similar $GdPc_2$ SMM [44]. Furthermore, estimating the splitting of anti-level crossings can be challenging, especially for lowly populated states. To gain further insight into the Zeeman diagram, the addition of electron paramagnetic resonance (EPR) will be demonstrated.

7.4. μ-SQUID - EPR

Using μ-SQUIDs as a magnetic probe in EPR experiments was demonstrated using a simplified setup to study photon-assisted tunneling in $S = 1/2$ systems such as Cr_7Ni [66], V_{15} [108] and the investigation of photon assisted tunneling in Fe_8 [109]. This technique has been further refined in the study of $Et_4N[^{160}GdPc_2]$ [44]. The following results aim to demonstrate the applicability of the new design for these measurements as well as gain insight into the spin system of the $^{160}Gd(tmhd)_3Phen$ SMM.

Using the APULN40 frequency synthesizer by Anapico allows the application of EM pulses triggered by the ADWin GoldII real-time measurement system, with pulse lengths from 10 ns up to continuous radiation with powers up to 20 dBm. The pulses are transmitted through a coaxial cable thermalized at various stages between room temperature and the 30 mK-stage, the sample holder, and the on-chip waveguide. For the chip design in transmission, the pulse is transmitted back to room temperature and absorbed at a 50 Ω load to avoid reflection back into the cryostat. Placing the SMM crystal in the proximity of the on-chip waveguide allows the application of resonant excitation via the generated pulse.

Figure 7.5 shows the magnetization curves at varying frequencies of the applied pulses at a sweeping rate of 8 mT/s. The pulses are applied at a power of 15 dBm at a width of 20 μs every 300 μs in between the switching current measurements of the μ-SQUID for the magnetization measurement. When satisfying the resonant condition: $h\nu = |E(m) - E(m')|$ allows photons' absorption and changes the spin states' population. The resulting change in magnetization can be detected by μ-SQUID , visible as peaks and dips in the magnetization curve.

The absorption peaks and dips can be extracted by applying a Gaussian filter to the magnetization curve, creating an artificial background, and subtracting this from the original. Plotting these against the applied frequency gives the spectrum shown in Figure 7.5. Here, the peaks and dips are highlighted in black and white against the orange background. The shadows around the appearing lines are an artifact from the extraction process. While the artifacts can be overcome by the usage of a percentile filter, the increase, in contrast, provides better visibility.

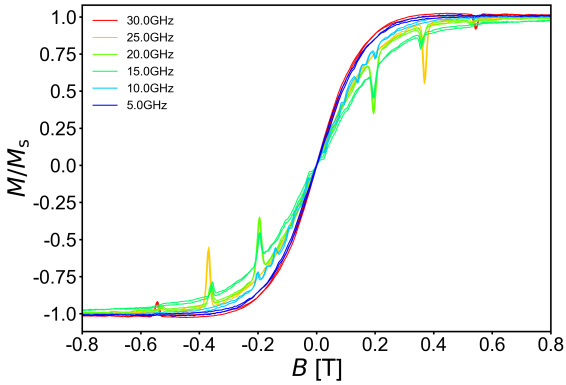

Figure 7.4. – Magnetization loops of a ^{160}Gd(tmhd)$_3$Phen single-molecule magnet crystal while irradiating with RF radiation at different frequencies. Matching the difference between energy levels with the energy of the irradiated photons allows for resonant absorption. The resulting distribution change of spins becomes visible as a change in magnetization. Therefore the dips and peaks in the magnetization curve indicate field values where levels of the Zeeman diagram are separated by the corresponding energy.

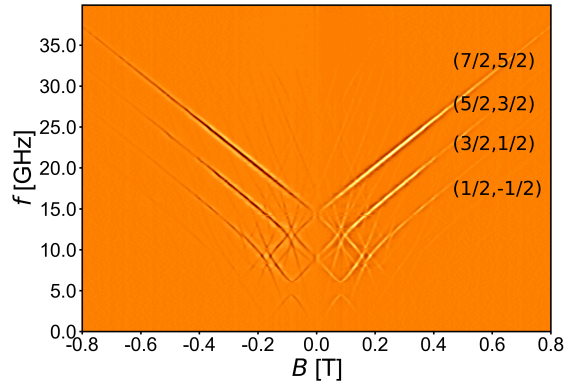

Figure 7.5. – EPR spectrum of the ^{160}Gd(tmhd)$_3$Phen single-molecule magnet. The resonances are visible as black and white lines against the orange background. The shadows next to the lines are an artifact due to the data treatment process. As the resonances represent differences in the energy levels of the Zeeman diagram, this allows the experimental determination of the Hamiltonian.

The high-field region allows us to the determination of the gyromagnetic ratio g, which is connected to the slope of these lines by

$$g = \frac{h}{\mu_B}\frac{dv}{dB} = 2.03 \tag{7.5}$$

Comparing with the literature value of g for the S-state ions, we get the main contributions:

- quantum electrodynamical value for the free electron: 2.0023
- mixing of ^{6}P excited state in the ground state $^8S_{7/2}$: -0.0078
- Judd and Lindgren relativistic contributions: -0.0017

resulting in the final theoretical value of $g = 1.992(8)$. This is already confirmed in various experiments on Gd^{3+} doped in inorganic lattices [110].

The experimental value of $g = 2.03$ differs from this theoretical prediction. While possible explanations for this difference can be investigated by taking higher-order Zeeman terms into account, the calibration of the 3D vector coil system has to be considered. As the measurements in Section 6.7 have shown that the x- and y-coil differ by 5 %, we have to assume a similar accuracy for the separate coils. Therefore the theoretical value is in the limit of the experimentally determined value $g = 2.03 \pm 0.1$.

7.5. Axial Interaction

The ligand field terms can be evaluated as a starting point using an axial approximation. By extrapolating the linear high field region of the (7/2, 5/2), (5/2, 3/2), (3/2, 1/2) transitions to zero field, the zero field splitting (ZFS) resonances can be derived . These will be denoted as ν_{01}, ν_{12}, ν_{23} referring to the transitions between the ground state and the respective excited states from the first to the third. Using the full expression of the three axial O^2_{2n} Steven operators, the spacing of the ZFS can be derived as

$$\begin{aligned} h\nu_{01} &= | \quad -6B_2^0 \quad +720B_4^0 \quad -17640B_6^0| \\ h\nu_{12} &= | \quad -12B_2^0 \quad +600B_4^0 \quad +17640B_6^0| \\ h\nu_{23} &= | \quad -18B_2^0 \quad +1200B_4^0 \quad +7560B_6^0| \end{aligned}$$

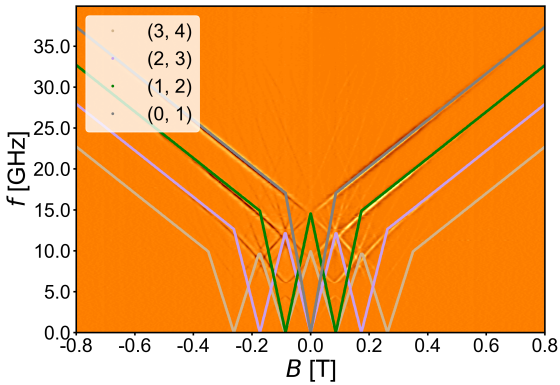

Figure 7.6. – EPR spectrum of the ^{160}Gd(tmhd)$_3$Phen single-molecule magnet compared with calculated resonances for selected transitions. The axial ligand field parameters used for simulation are determined by solving the system of linear equations created by calculating the influence of the axial ligand field parameters on the zero-field splitting resonances. The used parameters are $B_2^0 = -826$ MHz, $B_4^0 = 0.23$ MHz and $B_6^0 = 0.01$ MHz.

providing an exact solution for B_{2n}^2. As a result we get $B_2^0 = -826$ MHz, $B_4^0 = 0.23$ MHz and $B_6^0 = 0.01$ MHz. To validate the calculated values for the ligand field parameters, we compare the resonance map with the calculated resonances calculated for the given set of parameters as shown in Figure 7.6. This calculation of the resonances and all further calculations concerning EPR resonances and Zeeman spectra are performed using the MATLAB toolbox EasySpin [111], which provides a multitude of tools concerning calculations around spin systems and EPR.

7.6. Transverse Interaction

The influence from off-diagonal parameters in Equation 7.4 creates a mixing of the S_z eigenstates to form the eigenstates of H as a linear combination of $|m\rangle$. A perturbative approach is usually applied because the exact solution is often difficult to obtain.

Mixing the states $|m\rangle$ and $|m'\rangle$ by the transverse term of order k, $BS_{\pm}^k$ results in the following expression for the tunnel splitting:

$$\Delta_m^{m'} \approx B_2^0 S^2 [BS^k/(2B_2^0 S^2)]^{(m'-m)/k} \tag{7.6}$$

It is essential to note the spin parity effect, as mixing between the states $|m\rangle$ and $|m'\rangle$ is only possible if the difference $|m-m'|$ is a multiple of k. Therefore the admixture of levels increases for small values of m and at the crossings, where axial and transverse interactions become comparable in magnitude.

As this technique allows complete freedom of applying magnetic fields in the plane of the SQUID, we can access the non-axial ligand field parameters by applying transverse fields. This allows us to discuss two different types of measurements:

- keep the direction of the magnetic field and the applied transverse field constant while varying the applied frequency
- keep the applied frequency constant and change the direction of the magnetic field in the SQUID plane

The first type is shown in Figure 7.7. The resonance maps show the focus on an anti-level-crossing. The gap between the levels increases slowly due to the increased mixture of the spin states due to the applied transverse field.

The second type is shown in Figure 7.8. The resonance map depicts sweeps in different directions in the easy-hard-plane of the SMMs at a fixed frequency of 20 GHz. This angular dependence allows access to both the magnitude and sign of the ligand field parameters, compared to the tunnel splitting, which is independent of the sign.

7.7. Fitting Procedure

Using these resonance maps, the off-diagonal ligand field parameters can be determined by fitting the calculated resonances to the resonance map. As the influence of the transverse parameters induces the mixing of the spin states, the notation of (m, m') is not suitable anymore, requiring an improved notation. Therefore, we label the transitions ranked on the occurrence in the energy spectrum, starting with 0 as the ground state and numbering the excited stated with $n \in \mathbb{N}$ as the nth excited state. Starting with the lower energy state, we label the transitions as (j,k) with $j,k \in \mathbb{N}_0$ and $j < k$. This new notation is shown in Figure 7.6.

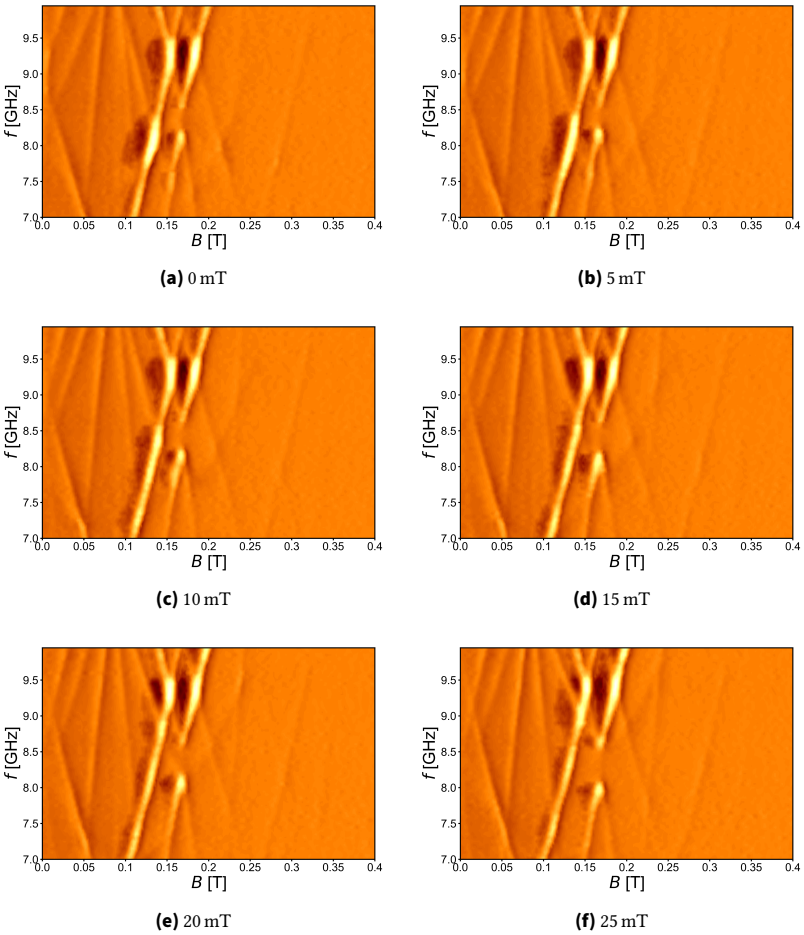

(a) 0 mT **(b)** 5 mT

(c) 10 mT **(d)** 15 mT

(e) 20 mT **(f)** 25 mT

Figure 7.7. – Cutout of the EPR spectra of the ^{160}Gd(tmhd)$_3$Phen SMM at different constant transverse fields perpendicular to the scanning direction. The avoided anti-level crossing opens up with an increasing transverse field. Fluctuations of the gap due to the Berry-Phase are not visible compared to the ^{157}GdPc$_2$ SMM [44].

Using this, we will further discuss the procedure to fit the resonance maps. As a basis, we use the g-value derived in Section 7.4 and the B_{2n}^2 ligand field parameters derived in Section 7.5 from the axial approximation. We assume the transverse ligand field parameters to be in the same order as the axial terms. After calculating the position of the resonances for a given set of parameters, we compare them to the experimental values. The deviation between calculated and experimental values is quantified by the distance between the closest pair of measured and computed resonance positions $\chi^2 = \sum(B_{x,exp} - B_{x,calc})^2 + (B_{y,exp} - B_{y,calc})^2$. The fitting is done by minimizing χ^2 in an iterative process using the Marquardt-Levenberg nonlinear algorithm with the fitting parameters: B_2^2, γ_1, γ_2.

The fitting is performed on the field map with 20 GHz, as shown in Figure 7.8f. As a result, we obtain $B_2^2 = -420$ MHz, $\gamma_1 = 8.4°$, and $\gamma_2 = 111.1°$ as parameters. To validate these parameters, we compare the field maps at 5 GHz and 10 GHz with the corresponding resonances as shown in Figure 7.8.

To further validate ligand field parameters, the second set of measurements has been performed in which the crystal is rotated by 90° to the side. In the resulting rotation, the easy axis is oriented perpendicular to the SQUID plane, resulting in a scan of the medium-hard plane.

Using the already acquired ligand field parameters, we use the 20 GHz field map again as a reference to fit the orientation of the spin in relation to the SQUID plane. The resulting angles are: $\gamma_1 = 97.1°$, $\gamma_2 = -8.1°$

Again, the validation with further field maps and the frequency map shows good correspondence with the experimental data.

7.8. Peak Heights

A remarkable feature lies in the height of the absorption peaks. Using the dependence of the magnetization on the spin

$$\vec{M} \propto \vec{\mu_S} = g_S \frac{q}{2m} \vec{S} \tag{7.7}$$

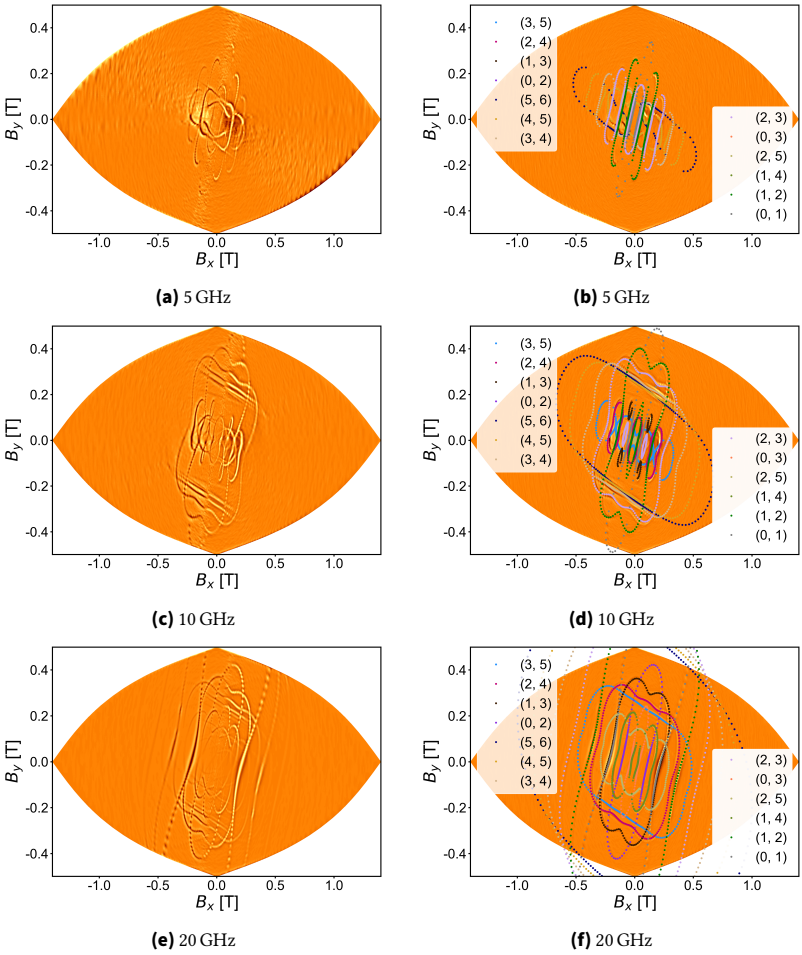

(a) 5 GHz **(b)** 5 GHz

(c) 10 GHz **(d)** 10 GHz

(e) 20 GHz **(f)** 20 GHz

Figure 7.8. – Angular dependence of the EPR spectra of the ^{160}Gd(tmhd)$_3$Phen SMM at a fixed frequency. The used parameters are: g = 2.03, γ_1= 8.4°, γ_2= 111.1°, B_2^0 = −826 MHz, B_2^2 = −420 MHz, B_4^0 = 0.23 MHz, B_6^0 = 0.01 MHz.

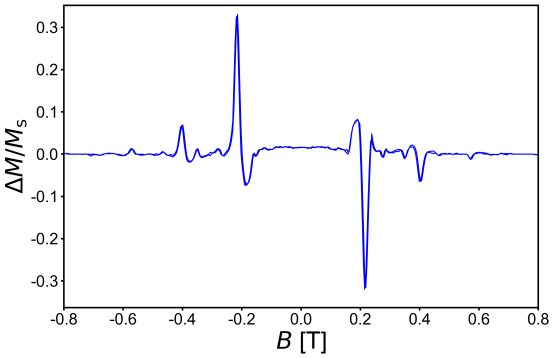

Figure 7.9. – Difference in magnetization between the magnetization during RF-excitation at 20 GHz and the estimated baseline of the $^{160}Gd(tmhd)_3Phen$ SMM. The change in magnetization exceeds the maximum estimated change.

we get the correlation of $\frac{\Delta M}{M_S} = \frac{\Delta S}{S}$. Using the (7/2, 5/2) transition as example, we'd get $\frac{\Delta M}{M_S} = \frac{2}{7}$. Furthermore, we have to consider that in equilibrium, the population of $S_Z = 5/2$ will be lower than 1/2 we get

$$\frac{\Delta M}{M_S} < \frac{1}{7} \approx 0.14. \tag{7.8}$$

Comparing this with Figure 7.9 shows the experimental magnetization change exceeds this limit with $\frac{\Delta M}{M_S} \approx 0.33$.

8. Summary and Outlook

This thesis presents different improvements in magnetometry based on superconducting μ-SQUIDs , and the extension of capabilities is demonstrated. Even with the long history of this technique, these improvements open further unexplored applications.

The first improvements concern the use of superconducting niobium nitride in this setting. The strong superconductivity of NbN to withstand high in-plane magnetic fields and high temperatures a set of SQUIDs has been fabricated using electron beam lithography and characterized to compare against the SQUIDs made out of niobium, which is the current state-of-the-art for this technique. These SQUIDs are shown to provide an extended temperature range, allowing temperature-dependent measurements up to 12 K while suffering reduced sensitivity due to the high kinetic inductance inherent to the material. In the limited range of the magnetic in-plane field of this setup, the niobium nitride provides similar capabilities to the pure niobium. As a final demonstration, the temperature dependence of a $Bi_{24}Mn_6$ SMM is measured.

To provide the capability for spin manipulation using RF radiation between DC and 40 GHz and a new sample holder and SQUIDs were fabricated. These allow strong coupling between the radiation and the molecules using an on-chip waveguide while using a readout via the magnetic signal. The implementation of this compact design allows integration into the 3D vector coil setup, allowing freedom of the direction of the applied magnetic field. The broadband capabilities and strong coupling could be demonstrated by analyzing the absorption of the Cr_7Ni Spin 1/2 SMM.

As a final application, the setup is used to perform EPR spectroscopy on a crystal of the $^{160}Gd(tmhd)_3Phen$ SMM. Using the broadband capability of the new setup and the flexibility in the direction of the applied magnetic field allows us to determine the strong influence of the basic ligand field parameters

while opening the possibility of determining higher-order parameters. These have been verified by comparing results with a rotated crystal.

While not being discussed in detail, the fast cooldown times of the Sionludino cryostat allows insight into a multitude of other SMMs as presented in [112–119].

The results of this thesis open the prospect of new experiments. The newly fabricated SQUIDs made from NbN allow for measurements of magnetic objects with exciting properties in the temperature range up to 12 K, such as particles of Nb, FeS, and SMMs with higher temperature stability.

The combination of magnetometry and RF radiation allows the investigation of further interactions. As such, the coherent manipulation of electronic and nuclear spin can path the road to quantum computation based on molecular magnets. The knowledge gained from the construction of this setup can be further used in combination with higher frequency radiation up to the visible spectrum to probe molecules with higher zero-field splitting.

Combining these approaches with the results gained from the EPR spectroscopy of the $^{160}Gd(tmhd)_3Phen$ SMM provides a deeper understanding of these molecules and helps to find suitable candidates for all quantum information applications.

List of Publications

1. Gheorghe Taran et al. « Direct determination of high-order transverse ligand field parameters via μSQUID-EPR in a Et4N [160GdPc2] SMM ». in: *Nature Communications* 14.1 (2023), p. 3361
2. Konstantinos Karachousos-Spiliotakopoulos et al. « Luminescence thermometry and field induced slow magnetic relaxation based on a near infrared emissive heterometallic complex ». In: *Dalton Transactions* 51.21 (2022), pp. 8208–8216
3. Konstantinos Karachousos-Spiliotakopoulos et al. « Lanthanide Luminescence Thermometry and Slow Magnetic Relaxation in 3-D Polycyanidometallate-Based Materials ». In: *Inorganic Chemistry* 61.46 (2022), pp. 18629–18639
4. Vassilis Tangoulis et al. « High-Performance Luminescence Thermometer with Field-Induced Slow Magnetic Relaxation Based on a Heterometallic Cyanido-Bridged 3d–4f Complex ». In: *Inorganic Chemistry* 61.5 (2022), pp. 2546–2557
5. Katerina Skordi et al. « High nuclearity structurally–related Mn supertetrahedral T4 aggregates ». In: *Chemical Communications* 57.93 (2021), pp. 12484–12487
6. Li Zhong et al. « Unprecedented one-dimensional chain and two-dimensional network dysprosium (III) single-molecule toroics with white-light emission ». In: *Chemical Communications* 56.17 (2020), pp. 2590–2593
7. Avik Bhanja et al. « Selective coordination of self-assembled hexanuclear [Ni4Ln2] and [Ni2Mn2Ln2](Ln= DyIII, TbIII, and HoIII) complexes: stepwise synthesis, structures, and magnetic properties ». In: *Inorganic Chemistry* 59.24 (2020), pp. 17929–17944
8. Hagen Kaemmerer et al. « Inorganic approach to stabilizing nanoscale toroidicity in a tetraicosanuclear Fe18Dy6 single molecule magnet ». In: *Journal of the American Chemical Society* 142.35 (2020), pp. 14838–14842

9. Sandeep K Gupta et al. « A single-ion single-electron cerrous magnet ». In: *Dalton Transactions* 48.42 (2019), pp. 15928–15935

A. Appendix A

A.1. Negative Resist ma-n 2401

description	equipment	parameters
spincoating ma-n 2401	spincoater	3000 rpm, 30 s
prebake	hotplate	90 °C, 60 s
exposure	Jeol JBX-5500FS	140 $\mu C/cm^2$
development	ma-D525	11 s
reactive ion etching	Etchlab 200	20 sccm, 13 Pa, 500 W, 11 s
restist removal	NMP	90 °C

A.2. Negative Resist AZ5214-E

description	equipment	parameters
spincoating AZ5214-E1	spincoater	6000 rpm, 60 s
prebake	hotplate	110 °C, 50 s
exposure	Suess Maskaligner	power 13, 3 s
postbake	hotplate	120 °C, 60 s
exposure	Suess Maskaligner	flood exposure, 30 s
development	AZ Developer: Water @ 1:1	40 s
lift-off	acetone	2 min

B. Appendix B

While the Sionludi cryostat is optimized to provide temperatures down to tens of mK, temperature-dependent measurements shown in this thesis require different capabilities, such as controlled and stable temperatures up to 12 K. As tuning the cooling power of this system requires extensive work for fine-tuning all operating parameters, the best approach shows to be compensating for the excess cooling power with controlled heating. A new system has been designed, tested, and implemented as the existing MGC3 by Cryoconcept showed various issues, such as restricted tunability and sudden working halts.

The system is based on the ESP32 32-Bit microcontroller by Espressif integrated into the ESP32-POE-ISO-EA (ESP32) board by Olimex. An essential advantage of this system is the capability of Power over Ethernet (PoE), which allows for double-use of the Ethernet connection for both power supply and integration with the whole system, avoiding the necessity of an additional power supply.

The board connects through the SPI interface to an external AD5662 16-bit DAC to apply a controlled voltage. This voltage gets passed on to a 1 kΩ -resistor connected to the cold plate to provide the controlled heating needed for stable temperatures. This increased temperature gets measured by the MMR3 module from Cryoconcept as described in Chapter 4. Using the TCP protocol, the measured temperature can be read by the ESP32 board. To provide a stable and controlled temperature of the cold plate, the microcontroller uses the temperature for a PID control loop to reach and hold a specified setpoint. This feedback loop is illustrated in Figure B.1. The complete schematic is shown in Appendix C.

To simplify the interaction with the heating module, the micro-controller provides a server to host a web page used to display and change essential parameters, such as applied power, the temperature setpoint, and the parameters for the PID loop. Interfacing can be done by TCP connection as

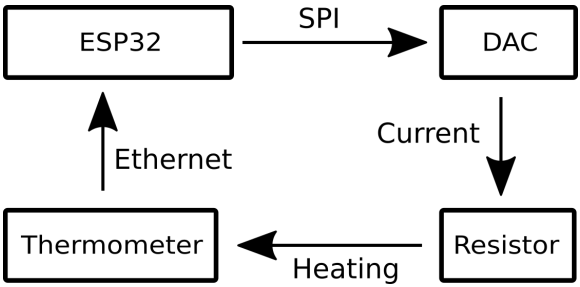

Figure B.1. – Feedback loop for the customized heating system. The ESP32 microcontroller sends the signal to the AD5662 16-bit DAC via SPI. The output voltage creates a current through the resistor inside the cryostat, resulting in heating the cold plate. The resulting temperature change can be measured by the MMR3 thermometer and read by the microcontroller. Using a PID control sequence allows for fast response and stable temperatures.

well. All transmission protocols are chosen for their reliability, simplicity in implementation, and sufficient transmission rate.

As measurements have shown, small heat input is provided even for zero applied voltage. Therefore a MOSFET switch and a 15 µF capacitor have been added to eliminate any heating if the setpoint is set to zero.

For stability and shielding, an aluminum casing has been added.

The fabrication of the circuit board and the casing were performed in the Electronic workshop and the Mechanical Workshop of the Physikalisches Institut of the Karlsruhe Institute of Technology, respectively.

The final device is shown in Figure B.2.

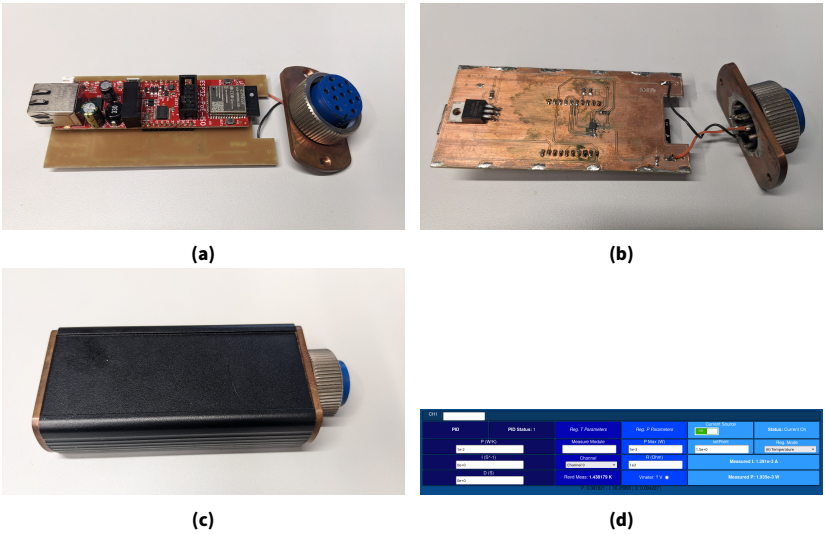

Figure B.2. – Final version of the newly built temperature control system. a) shows the top of the circuit board, featuring the ESP32-POE-ISO-EA (ESP32) board by Olimex. b) shows the bottom of the circuit board contains all additional electronic components. c) shows the device packaged in the aluminum casing. d) shows the user interface for control via the Ethernet network.

C. Appendix C

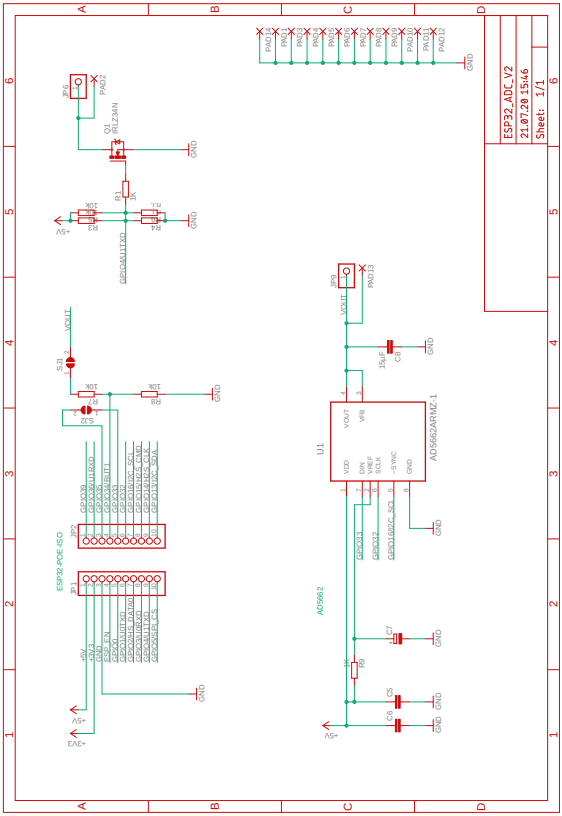
ESP32_ADC_V2
21.07.20 15:46
Sheet: 1/1
AD5662
AD5662ARMZ-1
ESP32-POE-ISO